

UCID-20473

VAULT REFERENCE COPY

ELF/VLF COMMUNICATIONS THROUGH THE EARTH
PROJECT REPORT FOR CALENDAR YEAR 1984

H. M. Buettner
G. J. Burke
E. M. Didwall
G. Holladay
R. J. Lytle

June 1985

Lawrence
Livermore
National
Laboratory

This is an internal report intended primarily for internal or limited external distribution. The opinions and conclusions stated are those of the author and may or may not be those of the Laboratory.

Work performed under the auspices of the U.S. Department of Energy by the Lawrence Livermore National Laboratory under Contract W-7405-Eng-48.

DISCLAIMER

This document was prepared as an account of work sponsored by an agency of the United States Government. Neither the United States Government nor the University of California nor any of their employees, makes any warranty, express or implied, or assumes any legal liability or responsibility for the accuracy, completeness, or usefulness of any information, apparatus, product, or process disclosed, or represents that its use would not infringe privately owned rights. Reference herein to any specific commercial products, process, or service by trade name, trademark, manufacturer, or otherwise, does not necessarily constitute or imply its endorsement, recommendation, or favoring by the United States Government or the University of California. The views and opinions of authors expressed herein do not necessarily state or reflect those of the United States Government or the University of California, and shall not be used for advertising or product endorsement purposes.

Printed in the United States of America
Available from
National Technical Information Service
U.S. Department of Commerce
5285 Port Royal Road
Springfield, VA 22161
Price: Printed Copy \$; Microfiche \$4.50

Page Range	Domestic Price	Page Range	Domestic Price
001-025	\$ 7.00	326-350	\$ 26.50
026-050	8.50	351-375	28.00
051-075	10.00	376-400	29.50
076-100	11.50	401-426	31.00
101-125	13.00	427-450	32.50
126-150	14.50	451-475	34.00
151-175	16.00	476-500	35.50
176-200	17.50	501-525	37.00
201-225	19.00	526-550	38.50
226-250	20.50	551-575	40.00
251-275	22.00	576-600	41.50
276-300	23.50	601-up ¹	
301-325	25.00		

¹Add 1.50 for each additional 25 page increment, or portion thereof from 601 pages up.

ELF-VLF COMMUNICATIONS THROUGH THE EARTH
PROJECT REPORT FOR CALENDAR YEAR 1984

Principal Investigators:

E.M. Didwall
R. J. Lytle

Prepared by:

H. M. Buettner
G. J. Burke
E. M. Didwall
G. Holladay
R. J. Lytle

Electronics Engineering Department
Lawrence Livermore National Laboratory

Prepared for the Headquarters,
Ballistic Missile Office, USAF
AF MIPR. NO. FY7653-84-04004

CONTENTS

	<u>Page</u>
Notation	iii
Executive Summary.....	v
Abstract	1
1. Introduction.....	1
2. Numerical Modeling of Subsurface Communication.....	2
2.1. The Point Source in a Half Space.....	3
2.2. Fields in Stratified Media.....	6
2.3. Current on a Finite Antenna.....	9
2.4. Results for Buried Sources.....	14
2.4.1. Fields of Point-Dipole Sources.....	14
2.4.2. Insulated Dipole Antennas.....	20
2.4.3. Summary of Numerical Modeling.....	26
3. Experimental Results.....	27
3.1. Goals of the Experimental Program.....	27
3.2. Yosemite Experiment.....	28
3.2.1. Location and Site Description.....	28
3.2.2. Summary of Experiments at Yosemite.....	28
3.3. Lake Lynn Laboratory Experiments.....	29
3.3.1. Location and Site Description.....	29
3.3.2. Summary of Experiments at LLL.....	29
3.3.3. Experimental Results and Discussion.....	33

CONTENTS (Continued)

	<u>Page</u>
3.3.4 An Estimate of Channel Capacity at LLL.....	48
3.3.5. Conclusions from Work at LLL.....	58
3.4. Experiments at National Underground Storage, Inc.....	59
3.4.1. Location and Site Description.....	59
3.4.2. Summary of Experiments at NUS.....	62
3.4.3. Experimental Results and Discussion.....	62
3.4.4. An Estimate of Channel Capacity for NUS.....	74
3.4.5. Conclusions from Work at NUS.....	76
4. Concluding Remarks.....	76
5. Acknowledgments.....	78
6. References.....	78

NOTATION

A	ampere
dB	$dB = 10 \log \frac{P_1}{P_0}$ or $dB = 20 \log \frac{V_1}{V_0}$ for voltage
\vec{E}	electric field intensity (volt/meter)
\vec{H}	magnetic field intensity (ampere/meter)
$H_0^{(2)}, H_1^{(2)}$	Hankel functions of the second kind*
I	electric current
\vec{J}	electric dipole moment
J_0	Bessel function
j	$\sqrt{-1}$
k	complex wave number
LLL	Lake Lynn Laboratory
LLNL	Lawrence Livermore National Laboratory
ℓ	length, in meters
\vec{M}	magnetic moment
m	meters
NUS	National Underground Storage
S	siemens (conductance)
s	seconds
$\left. \begin{matrix} U \\ V \end{matrix} \right\}$	potentials
V_0	voltage

* Use the convention, $e^{j\omega t}$.

$\begin{matrix} x \\ y \end{matrix} \}$	horizontal components in Cartesian coordinates
z	vertical component in Cartesian or cylindrical coordinates
Z	impedance
ϵ	dielectric constant
ϵ_0	dielectric constant for free space
γ_{\pm}	function $\gamma_{\pm} = (\lambda^2 - k_{\pm}^2)^{1/2}$
λ	wavelength
μ	magnetic permeability
μ_0	magnetic permeability in free space
Π	Hertz potential
π	~ 3.1415
ρ	rho component in cylindrical coordinates
σ	conductivity (S/m)
ϕ	angular coordinate in cylindrical coordinates
ω	angular frequency, $2\pi f$

EXECUTIVE SUMMARY

One concern in deep-basing strategy is communications, particularly in a post-nuclear-attack environment. One candidate means of communication would depend on "through-the-Earth" electromagnetic (EM) propagation without a surface antenna directly linked to the underground base. Electromagnetic propagation in the ELF to VLF range offers the possibility of establishing a communications link from the underground base to the surface with a minimum binary bit rate of 75 bits per second; higher bit rates may be possible. Nominally, we will investigate EM propagation in the 200 Hz-30 kHz frequency ranges.

We are evaluating through-the-Earth communication by theoretical and experimental means. By developing computer codes, we can address hypothetical antenna-placement schemes, where a transmission antenna is placed underground and a receiving antenna is placed on the Earth's surface or on an airborne platform. By performing field experiments, we can acquire data for specific geological types, demonstrate communication at depth, and provide test cases for the computer models. In addition, field experiments highlight practical problems in the design and placement of a transmitter-receiver system. Determination of the maximum frequency suitable for through-the-Earth communication will help to determine the maximum bit rate for the system. Also, for selected experiment sites, the propagation experiments will yield an experimental determination of electrical properties.

The computer modeling and experimental work, sponsored in 1984 by the Headquarters, Ballistic Missile Office (HQ BMO) of the United States Air Force, achieved some promising results. The basic modeling requirements

needed to evaluate effects of conductivity and the air-earth interface were met. Prompted by inquiries from the Air Force and its contractors, we proceeded to evaluate multilayered effects and started to evaluate wire insulation effects. Early in the experimental work, we found that we would have to develop a means of verifying that the signal propagates through rock and not through some unsuspected path to the surface-based receivers. In October, 1984, we utilized methods for evaluating signal propagation through limestone and interbedded sedimentary formations located at the Lake Lynn Laboratory (LLL) and the National Underground Storage (NUS) facility. We found that "sneak-through" paths for certain experimental arrangements allowed greater signal strengths to propagate than could be expected from pure through-the-Earth communication. However, our methodology also demonstrated cases when propagation was predominantly through the Earth, as in the surface-to-subsurface transmission at LLL. These results were consistent with those of computer-generated models. By comparing experimental values with computer-generated plots, we estimated attenuation and conductivity values for the rock.

We used our experimental data to estimate maximum-channel capacity for receiver depths of 100-500 m (328-1640 ft). Results up to 300 m (984 ft) are very promising, with theoretical channel capacities of the order of kbits/s for a transmitter of modest physical size. However, these estimates represent a maximum under a specific set of assumptions. Actual channel capacities will depend upon the noise figure and type, and the specific geologic and environmental setting. Also, the achievable bit rate and bit error rate are a function of the modulation scheme used to transmit the binary information.

However, these results do indicate that the minimum information rate of 75 bits/s should easily be achieved.

Further work planned for FY85 includes additional computer-model developments and a field experiment with a subsurface to surface distance greater than 305 m (1000 ft). Also, some consideration will be given to natural and man-made structures that may enhance through-the-Earth propagation.

ABSTRACT

We use computer models and experiments to explore the feasibility of communication between points underground and on the Earth's surface. Emphasis is placed on ELF-VLF electromagnetic propagation through the Earth; nominally, we investigated propagation in the 200 Hz-30 kHz frequency range. The computer modeling included calculations of the fields of a point electric or magnetic source in a homogeneous half space or a stratified earth. Initial results for an insulated antenna of finite length are also considered. The experiments involved through-the-Earth transmissions at two locations in Pennsylvania, both of which had large formations of limestone. Initial results indicate that information rates as high as kbits/s may be possible for subsurface depths of 300 m or less. Accuracy of these estimates depends on the electromagnetic propagation constants of the rock, the noise characteristics, and modulation scheme. Although a nuisance for evaluating through-the-Earth propagation, the existence of subsurface metal conductors can improve the transmission character of the site.

1. INTRODUCTION

Propagation of electromagnetic signals between a site buried in the Earth and a surface or airborne station is of interest for a number of applications. This through-the-Earth communication can be applied, for example, in communicating to underground facilities, locating trapped miners, and in detecting buried anomalies in the Earth. For communication to an underground facility, we wish to develop a methodology for evaluating the concept, for evaluating sites, and for experimentally demonstrating the concept.

Our approach to evaluating through-the-Earth communication includes theoretical and experimental means. By developing computer codes, we can address hypothetical schemes for situating a transmission antenna underground and a receiving antenna on the Earth's surface or on an airborne platform. With field experiments, we can acquire data for specific geological types, demonstrate communication at depth, and provide test cases for the computer models. In addition, field experiments highlight practical problems in the design and placement of a transmitter-receiver system. Determination of the maximum frequency suitable for through-the-Earth communication will help to determine the maximum bit rate for the system. Also, for selected experiment sites, the propagation experiments will yield an independent determination of electrical properties.

This report describes our results for the Calendar Year 1984.

2. NUMERICAL MODELING OF SUBSURFACE COMMUNICATION

Antennas used in the Earth are typically linear conductors, such as wires or pipes that form dipoles, loops, or more complex configurations. Buried antennas are usually insulated to improve their efficiency. Modeling of these antennas requires determination of the current on the antenna and evaluation of the field that this current produces at the receiver location.

The modeling approach discussed here is based on an evaluation of the field of a point source in the Earth. We give the exact integral expressions for the field of a point source in a homogeneous or stratified earth, and outline the numerical techniques used for evaluating these integrals.

To model a real antenna, its current distribution must be determined. Insulation can have a major effect on the current distribution but has little effect on the field produced by a given current at a distance. Two methods are considered for evaluating the current: 1) For a straight, insulated wire in the earth, the current can be approximated reasonably accurately by a sinusoidal distribution with the propagation factor along the wire determined from transmission line theory; and 2) On more complex structures, the current must be determined by numerical solution of an integral equation. The field of a point source is, again, the basis of this approach since it forms the kernel of the integral equation. The integral equation solution is not described in detail here but is contained in other reports (Burke and Miller, 1984).

Once the current has been determined, the radiated field can be computed by using the field of a point source and integrating over the current distribution. A more detailed description of these steps in the numerical modeling is discussed in the companion report, "Numerical Modeling of Subsurface Communication," by Burke, Dease, Didwall, and Lytle (1985).

2.1. THE POINT SOURCE IN A HALF SPACE

Sommerfeld (1909) developed the solution for the field of a point source in the ground. For this solution, the fields are expanded in cylindrical-wave functions, and boundary conditions are matched at the interface.

The resulting expressions for the field components are in the form of inverse Hankel transforms. The field on the opposite side of the interface from an electric dipole with moment $I\ell$ can be obtained from the potentials

$$V_{\pm}^T = 2 \int_0^{\infty} \frac{e^{-\gamma_{\pm}|z'| - \gamma_{\pm}|z|}}{k_{\pm}^2 \gamma_{\pm} + k_{\mp}^2 \gamma_{\mp}} J_0(\lambda \rho) \lambda d\lambda, \quad (1)$$

and

$$U_{\pm}^T = 2 \int_0^{\infty} \frac{e^{-\gamma_{\mp}|z'| - \gamma_{\pm}|z|}}{\gamma_{\mp} + \gamma_{\pm}} J_0(\lambda \rho) \lambda d\lambda, \quad (2)$$

for the field above (+) or below (-) the interface (Banos, 1966). Time dependence $e^{j\omega t}$ is assumed. The vertical coordinates of the source and field point are z' and z , respectively, and their horizontal separation is ρ . Also,

$$\gamma_{\pm} = (\lambda^2 - k_{\pm}^2)^{1/2},$$

and

$$k_{\pm} = \omega(\mu_0 \epsilon_0)^{1/2} \left(\epsilon_{\pm} - j \frac{\sigma_{\pm}}{\omega \epsilon_0} \right)^{1/2},$$

where ϵ_{\pm} and σ_{\pm} are the relative dielectric constant and the conductivity above or below the interface. The cylindrical components of electric field for a vertical electric dipole (V superscript) or horizontal electric dipole in the $\phi = 0$ direction (H superscript) are given by

$$E_{\pm\rho}^V = C_1 \frac{\partial^2}{\partial\rho\partial z} V_{\pm}^T ,$$

$$E_{\pm z}^V = C_1 \left(\frac{\partial^2}{\partial z^2} + k_{\pm}^2 \right) V_{\pm}^T ,$$

$$E_{\pm\rho}^H = C_1 \cos \phi \left(\frac{\partial^2}{\partial\rho^2} V_{\pm}^T + U_{\pm}^T \right) ,$$

$$E_{\pm\phi}^H = -C_1 \sin \phi \left(\frac{1}{\rho} \frac{\partial^2}{\partial\rho} V_{\pm}^T + U_{\pm}^T \right) ,$$

and

$$E_{\pm z}^H = -C_1 \cos \phi \frac{\partial^2}{\partial\rho\partial z'} V_{\pm}^T ,$$

where $C_1 = -j\omega\mu_0 I\ell/4\pi$.

The infinite integrals in Eqs. (1) and (2) cannot be evaluated in closed form. Approximations have been developed for various ranges of distance and medium parameters. However, approximating the field above the interface due to a source at a depth directly below is particularly difficult. Hence, the field components were obtained by numerical evaluation of the integral expressions.

The details of our numerical approach are described in a separate publication (Burke, Dease, Didwall, and Lytle, 1985).

2.2. FIELDS IN STRATIFIED MEDIA

The fields of a source in a stratified medium can be written as integrals similar in form to those for a half space. In the stratified medium, however, upward and downward propagating waves must be considered in each layer. The waves in the layer containing the source can be derived in terms of reflection coefficients at the interfaces bounding the layer. These reflection coefficients are determined from surface impedances obtained by cascading the input impedances of successive layers, a technique introduced by Wait (1953). Stoyer (1977) derived the complete equations for the fields in any layer due to an electric or magnetic dipole source with vertical or horizontal orientation. Stoyer's equations are used here, except that the equations for propagating the wave coefficients through successive layers have been modified to reduce numerical error.

The geometry of the stratified medium is shown in Fig. 1 where the source is at $z = -d$ in layer zero. Each layer is homogeneous and isotropic with permeability μ_i and complex conductivity σ_i' , where

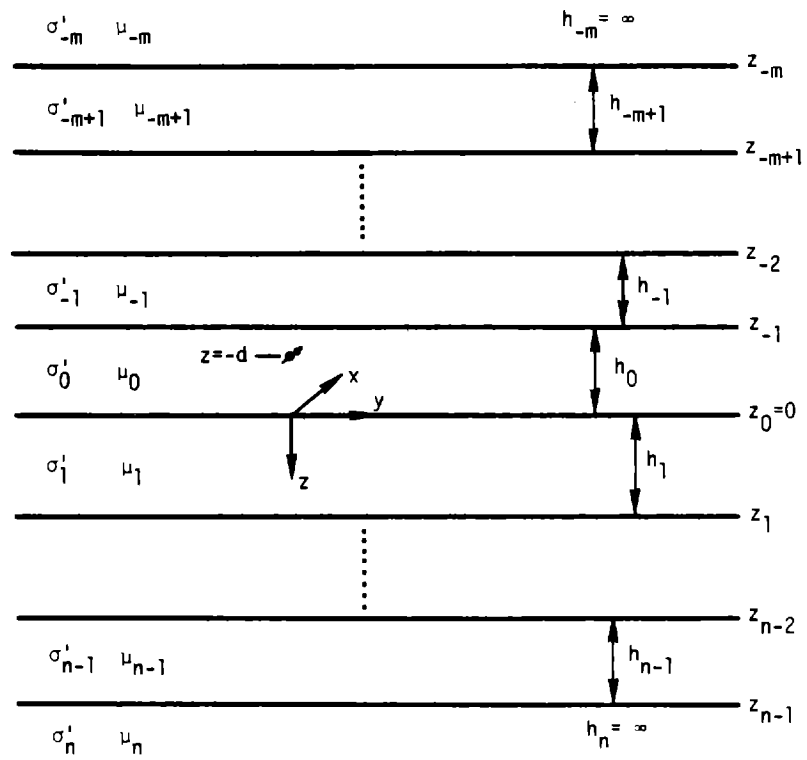


Figure 1. Parameters for a stratified medium with m interfaces above the source and n interfaces below the source. Source is at $z = -d$ in layer 0.

$$\sigma'_i = \sigma_i + j\omega\epsilon_i$$

and σ_i and ϵ_i are the conductivity and dielectric constants of layer i . The layer n below and layer $-m$ above the source layer are semi-infinite.

The fields can be obtained from a Hertz potential $\vec{\Pi}$, the components of which involve integrals similar in form to Eqs. 1 and 2. For a magnetic dipole source, the electric and magnetic fields are then obtained as

$$\begin{aligned} \mathbf{E} &= -j\omega\mu\nabla \times \vec{\Pi} \\ \mathbf{H} &= \nabla(\nabla \cdot \vec{\Pi}) + k^2\vec{\Pi} \end{aligned}$$

The fields of an electric dipole source can be obtained from the equations for the magnetic dipole through application of the duality principle. If the moment of the electric dipole is \vec{J} , the field can be obtained with the following replacement, from the previous equations for a magnetic dipole with moment \vec{M} :

Magnetic SourceElectric Source

$\sigma'_i \vec{M}$	\leftrightarrow	\vec{J}
$-j\omega\mu_i$	\leftrightarrow	σ'_i
\vec{H}	\leftrightarrow	\vec{E}
\vec{E}	\leftrightarrow	\vec{H}

2.3. CURRENT ON A FINITE ANTENNA

To determine the communication efficiency of a buried antenna, the size and shape of the antenna must be considered. A buried point source would have infinite input power and hence is not useful in considering efficiency. On an antenna of finite size, the distribution of current must be determined for a given source voltage. This can be a difficult problem for an isolated antenna and is made more so when the antenna interacts with an interface and may have an insulating sheath.

One approach is to solve an integral equation for the current. A number of computer codes that use the method of moments to reduce the integral equation to a matrix equation for numerical solution have been developed for this purpose. The kernel of the integral equation involves the field of a point source in the antenna environment. Hence, the previously discussed solution for the field of a point source in the ground is needed. An integral equation code has been developed at LLNL for modeling antennas above or below

the surface of a homogeneous ground (Burke, Miller, 1984). This code, however, will not presently model the insulated wires of interest for subsurface communication.

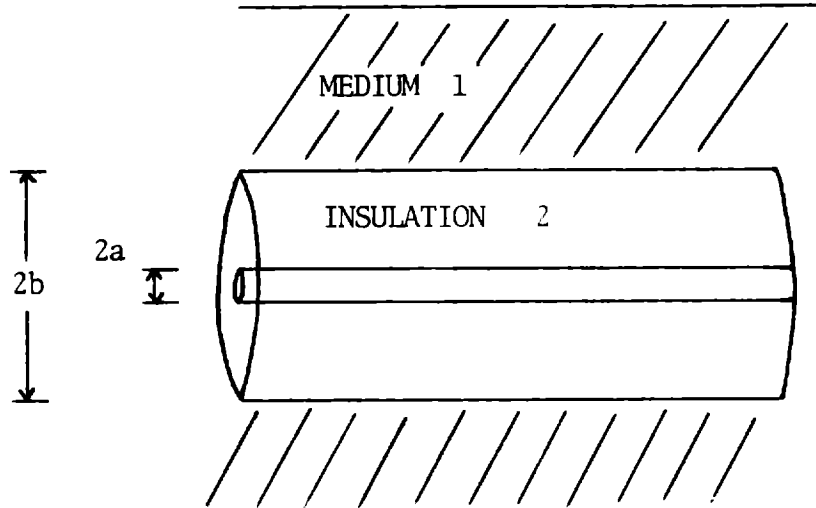
Another code, developed by Richmond (1973), will solve for the current on an insulated wire in an infinite lossy medium. The effect of the insulation is included in the integral equation as the field of a radial polarization current in the insulation volume. This code does not include the effect of the air-ground interface. The code can be used, however, to compute the current on deeply buried insulated wires of arbitrary shape.

A simpler way to determine the current is to assume a sinusoidal distribution with an appropriate propagation factor along the wire. This assumption can often yield reasonable accuracy for a straight wire. King (1981) shows, from the solution for current on a coaxial transmission line, that the wave number $\left(\frac{2\pi}{\text{wavelength}}\right)$ on a perfectly conducting wire of radius a and with an insulating sheath of radius b (medium 2) imbedded in an infinite conducting medium (medium 1), as shown in Fig. 2, is

$$k_L = k_2 \left[1 + \frac{H_0^{(2)}(k_1 b)}{k_1 b \ln(b/a) H_1^{(2)}(k_1 b)} \right]^{1/2} ,$$

where $k_1 = \omega \mu_0^{1/2} (\epsilon_1 - j\sigma_1/\omega)^{1/2} ,$

$$k_2 = \omega \mu_0^{1/2} (\epsilon_2 - j\sigma_2/\omega)^{1/2} ,$$



Propagation constant on an insulated wire is

$$k_L \approx k_2 \left[1 + \frac{H_0^{(2)}(k_1 b)}{k_1 b \ln(b/a) H_1^{(2)}(k_1 b)} \right]^{1/2}$$

For dipole with length $2h$ with insulated ends

$$Y_{in} = \frac{i}{2z_c} \tan(k_L h)$$

$$z_c = \frac{\omega \mu k_L}{2\pi k_2^2} \ln(b/a)$$

and the current distribution is

$$I(x) = \frac{iV_0}{2z_c} \frac{\sin k_L(h - |x|)}{\cos(k_L h)}$$

Figure 2. Insulated wire solution (from King, 1981).

and $H_0^{(2)}$ and $H_1^{(2)}$ are Hankel functions of order 0 and 1. This approximation is valid if

$$|k_1| \gg |k_2| ,$$

which is true for insulation in typical earth at low frequency.

On an insulated straight wire with open ends, the current goes to zero at the ends and can be assumed to vary sinusoidally along the wire with wave number k_L . If the wire has length $2h$ and is driven at its center with a voltage V_0 , the sinusoidal approximation of the current is

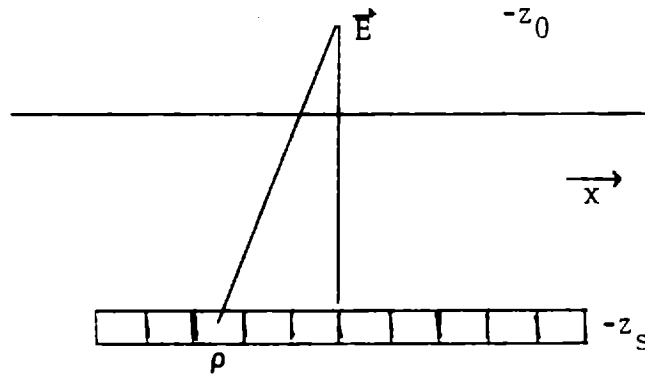
$$I(x) = \frac{i V_0}{2 Z_c} \frac{\sin[k_L(h - |x|)]}{\cos(k_L h)} ,$$

where Z_c is the characteristic impedance of the line:

$$Z_c = \frac{\omega \mu k_L}{2\pi k_2^2} \ln(b/a) .$$

The field at a receiver location (Fig. 3) produced by this current can be obtained by numerically integrating the product of the current and the field of a point source at each point along the dipole.

THE FIELD ABOVE THE GROUND IS OBTAINED
BY NUMERICALLY INTEGRATING OVER $I(x)$



Where $\vec{G}(\rho, z_s, z_0)$ involves Sommerfeld integrals that take account of medium parameters and interfaces

$$\vec{E} = \int_{-h}^h I(x) \vec{G}(\rho, z_s, z_0) dx$$

Figure 3. The field at a receiver location can be obtained by numerically integrating the product of the current and the field at a point source at each point along the dipole.

2.4. RESULTS FOR BURIED SOURCES

Some typical results of the models described previously are shown in this section. These idealized models can, in many cases, provide a good approximation to the real Earth environment. Modeling a "real" situation is difficult because there are many variables, many of which are unknown. Also, real situations may provide an abundance of mathematical difficulties. However, a reasonable evaluation of a real situation can be obtained by judiciously selecting the representative parameters.

2.4.1. Fields Of Point-Dipole Sources

The advantage of considering point sources is that the fields can be evaluated in considerably less time than the field of a finite antenna, which requires summation over many point sources. Also, the results are more easily understood in terms of propagation through the Earth. Although input power cannot be evaluated, the point-source models can demonstrate the relative difficulty of communicating for specific frequencies, source types, and field orientations. The codes will model either electric or magnetic point dipoles, which represent electrically small dipole or loop antennas, respectively.

Results for the surface field due to a point source at depth in a half space were generated for various earth conductivities and frequencies. For the frequencies of interest (ELF to VLF) and typical conductivities of rock, conduction currents dominate in the ground. Hence, the dielectric constant of the ground has little effect and was held constant at $\epsilon_r = 10$.

Typical results are shown in Figs. 4 and 5 for transmissions at 1 kHz from a source at 305 m (1000 ft) depth in a half space consisting of rock with

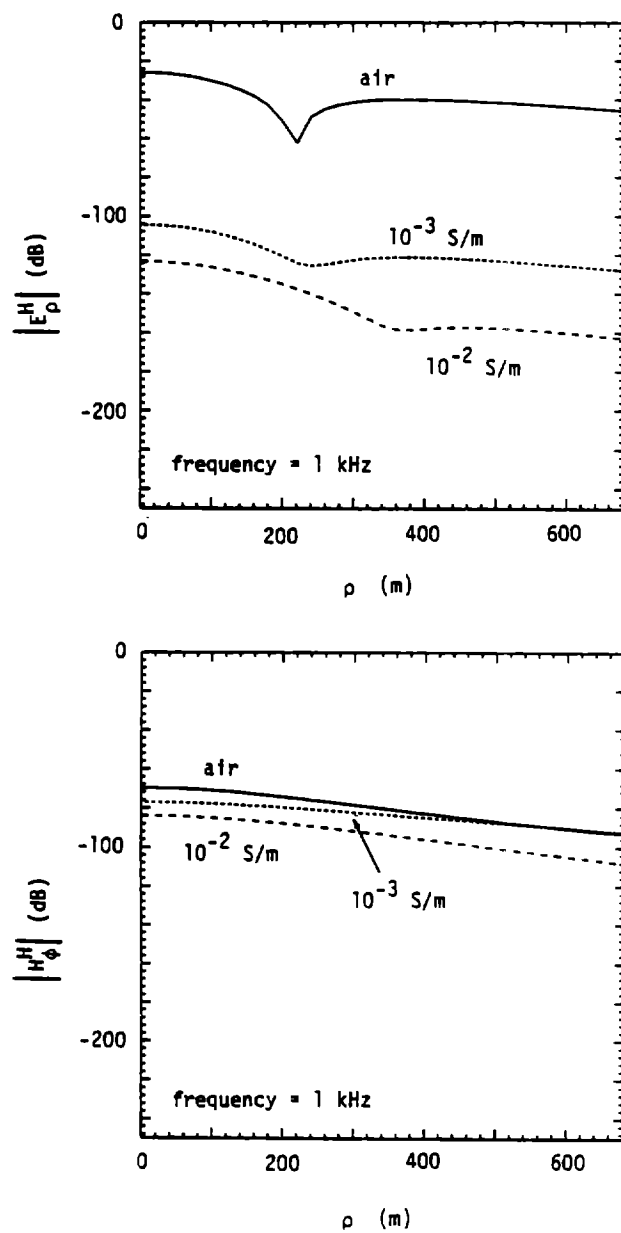


Figure 4. Horizontal electric and magnetic fields in air above a horizontal unit electric dipole source at a depth of 305 m (1000 ft). Ground conductivities of 10^{-2} and 10^{-3} S/m are shown. The field when the ground is replaced by air is included as a reference.

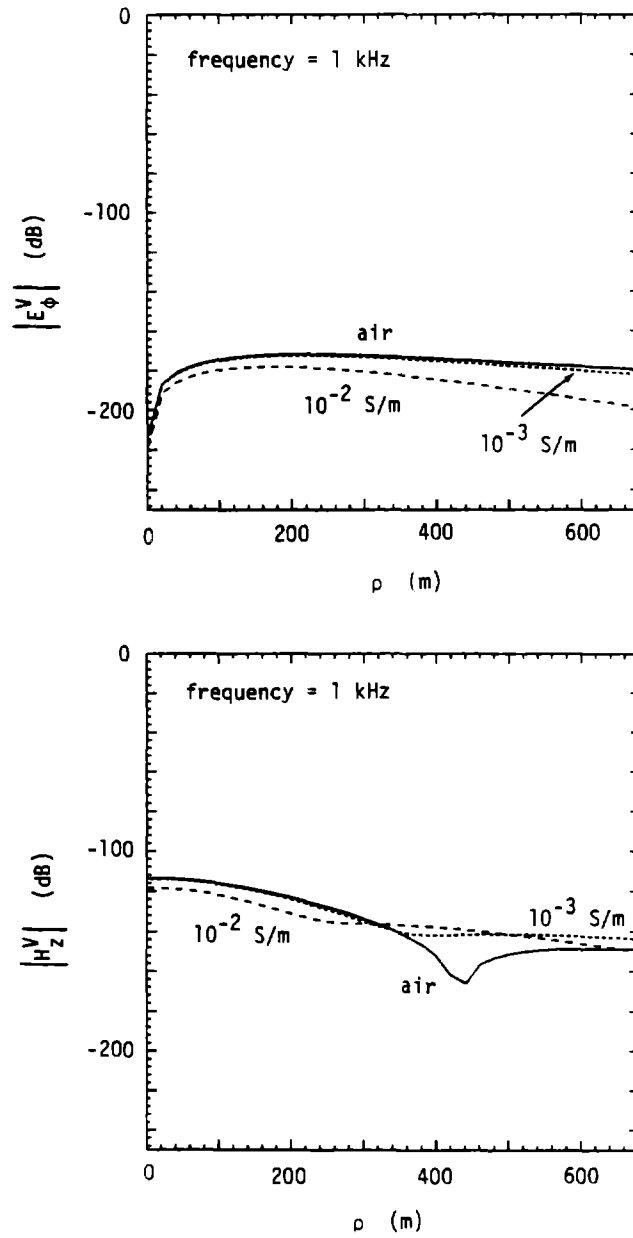


Figure 5. Horizontal electric field and vertical magnetic field in air above a vertical unit magnetic dipole source.

two values of conductivity. The field transmitted through air is shown as a reference. The electric dipole source had a strength of $1 \text{ A}\cdot\text{m}$ and the magnetic dipole strength was $1 \text{ A}\cdot\text{m}^2$. The plots for varying lateral separation of transmitter and receiver (ρ) show the effect of the receiver being displaced from a point directly over the source. Also, these results show the effect of attenuation through the rock and the effect of medium parameters on the ratio of electric to magnetic field strength for a given source. The electric field transmitted through the Earth with a conductivity of 10^{-3} S/m from a horizontal electric dipole (Fig. 4) is reduced by about 80 dB relative to transmission through air. A similar calculation for the magnetic field of a magnetic dipole source (Fig. 5) indicates almost no change relative to transmission through air. These results indicate that the attenuation is relatively small for this frequency and distance. The reduction of electric field strength is related to the characteristic impedance of the medium and would show little change if the transmission distance was reduced.

For depths of 305 m (1000 ft) or more, the Earth is rarely a homogeneous medium. Often there are layers of different rock types with varying water saturations and, most likely, different electrical conductivities. The model developed for a point source in a layered medium can approximate these real situations with the restrictions that the layers are horizontal and have no lateral variation.

The parameters of layered ground that we considered are shown in Fig. 6. The depth of each layer is given with a possible range of conductivities. The computed magnetic field at the surface is shown in Fig. 7 for a vertical magnetic dipole source at a depth of 305 m (1000 ft). The

IN GENERIC MOUNTAIN C, THE FIRST
2500 FEET CONTAIN BOTH IGNEOUS & SEDIMENTARY
STRUCTURES

UNIT	DEPTH
1 basaltic caprock $\sigma=0.01-0.1$ S/m	0'-200'
2 pyroclastic rock $\sigma=0.002-0.07$ S/m	200'-(750-1200)'
3 interbedded silty limestone, tuff, etc. $\sigma=0.1-1.0$ S/m	(750-1200)'- (1000-1750)'
4 interbedded shaly sandstone, sandy shale, etc. $\sigma=0.05-0.2$ S/m	(1000-1750)'- (1000-1900)'
5 sandstone, mudstone, etc. $\sigma=0.01-0.04$ S/m	(1000-1900)'- (1450-3100)'

Conductivity values from preliminary
draft of "ICBM Deep Basing Construction
Planning Study, Geology Report," Corps
of Engineers, Omaha District, April 1984.

Figure 6. Generic Mountain C--The model used for "stratified Earth" in
numerical calculations.

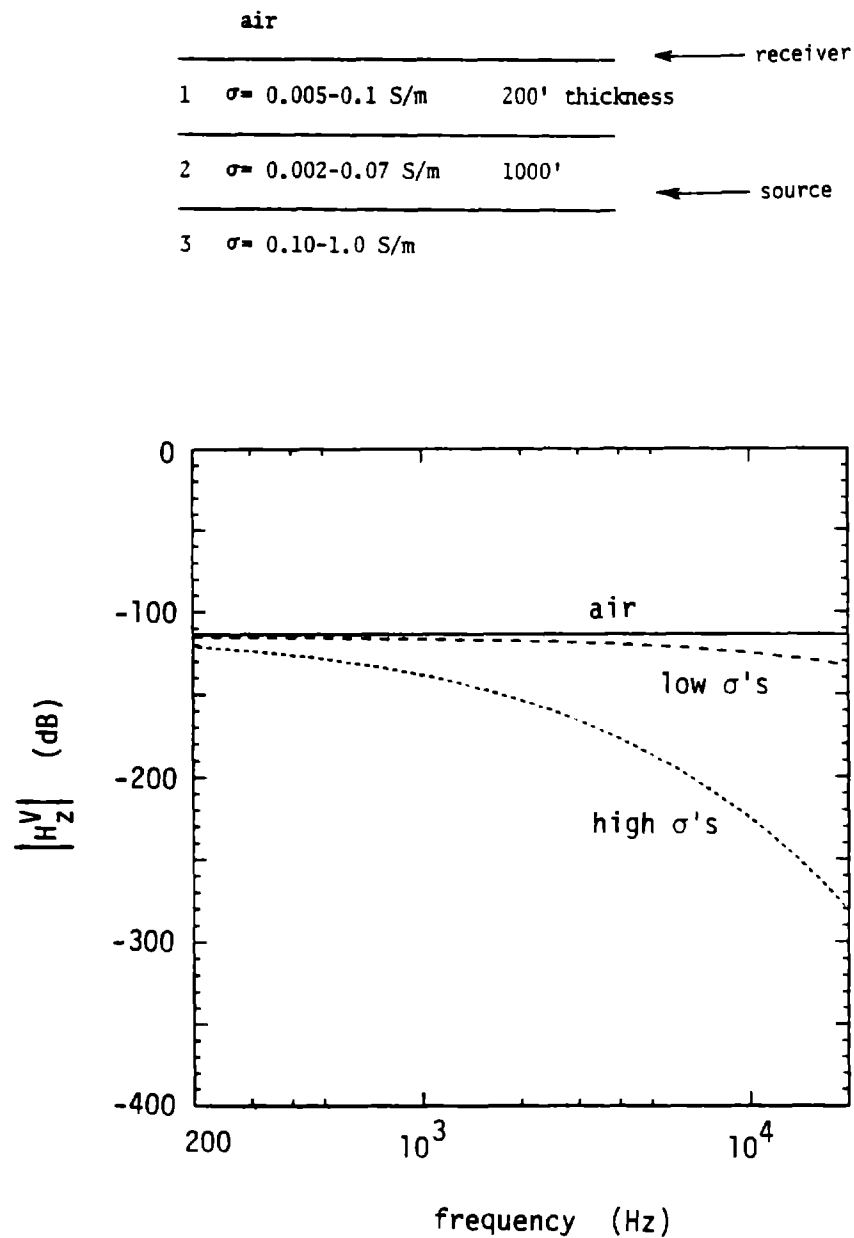


Figure 7. The vertical magnetic field above the Earth is shown for a vertical magnetic dipole source at a depth of 305 m (1000 ft) in a stratified medium. Results for the low and high limits of the range of conductivities show the best and worst cases for communication.

field at the same distance in air is shown for comparison. From these results, communication to a 305 m (1000 ft) depth looks promising for frequencies up to 1 kHz and possibly higher, depending on true conductivities and the transmitter efficiency.

In Fig. 8, the field strength is shown for a transmitter depth of 762 m (2500 ft). In this case, possible variations in layer thicknesses as well as conductivities were considered. Communication to 762 m appears practical at low frequencies. The upper limit on frequency would depend strongly on the actual Earth parameters relative to the best and worst cases modeled.

2.4.2. Insulated Dipole Antennas

An actual transmission antenna will not be an infinitesimal dipole as represented by the unit-dipole source. Instead, it will be an antenna of finite length. In addition, it will probably be insulated from the ground as, for example, a wire in an air-filled tunnel. Insulation can greatly reduce the power dissipated in the Earth immediately surrounding the antenna and, hence, can increase the field strength at the surface for a given input power.

When the approximate current distribution on a buried insulated dipole is computed as described in Sec. 2.3., the input impedance and input power can be determined. Thus, the field strength at a receiver location can be computed for a given input power rather than for a constant dipole moment as was done for a point source. Also, the problem of matching the antenna to the transmitter can be considered.

The calculated electric field above the ground from a buried insulated dipole is shown in Fig. 9. The ends of the dipole were not grounded. Field

air			← receiver
1	$\sigma=0.005-0.1$ S/m	200' thickness	
2	$\sigma=0.002-0.07$ S/m	1000'	
3	$\sigma=0.10-1.0$ S/m	750'	
4	$\sigma=0.05-0.2$ S/m	150'	
5	$\sigma=0.01-0.04$ S/m	1200'	← source
6	$\sigma=0.05-0.2$ S/m		

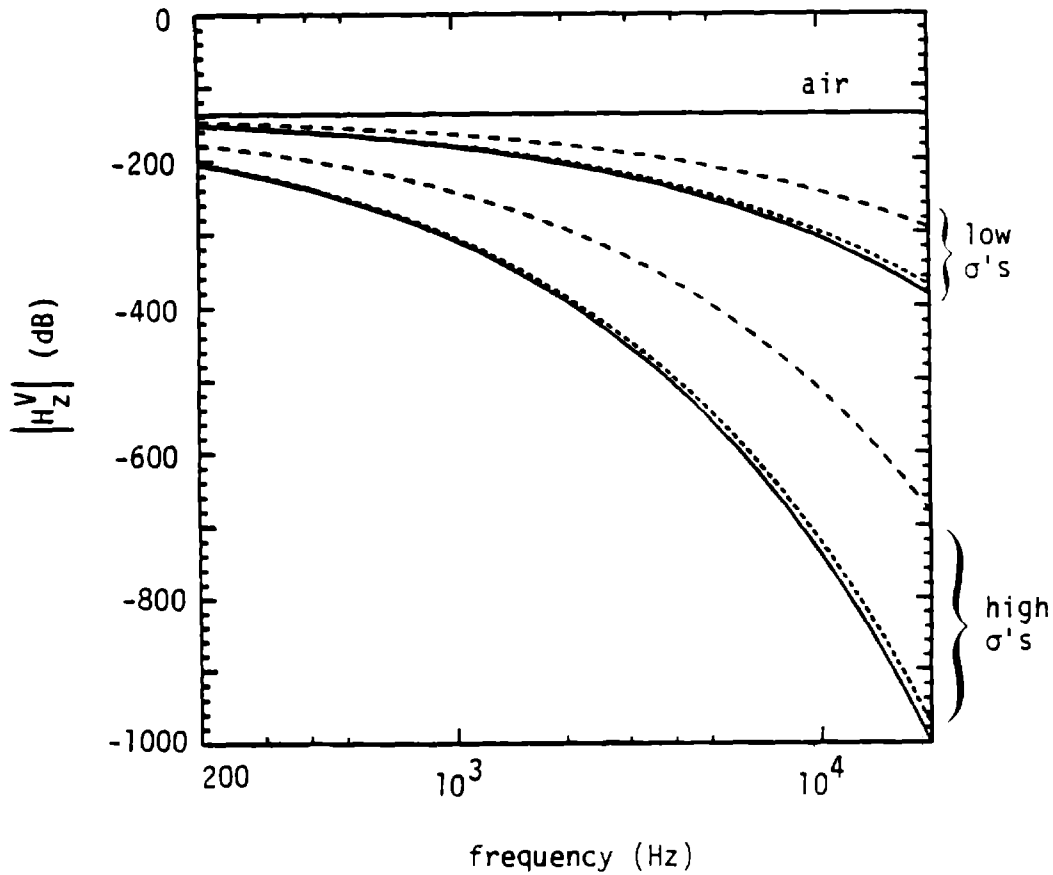


Figure 8. The vertical magnetic field is shown above a vertical magnetic dipole source at a depth of 762 m (2500 ft) in a stratified medium. Variations in layer thicknesses, as well as conductivities, were considered in the range from best to worst cases. Results include the model shown above (—), model with thickness of layer 4 = 0 m (-----), and model with thickness of layer 4 = 0 m and thickness of layer 3 = 76.2 m (250 ft) (~~~~~).

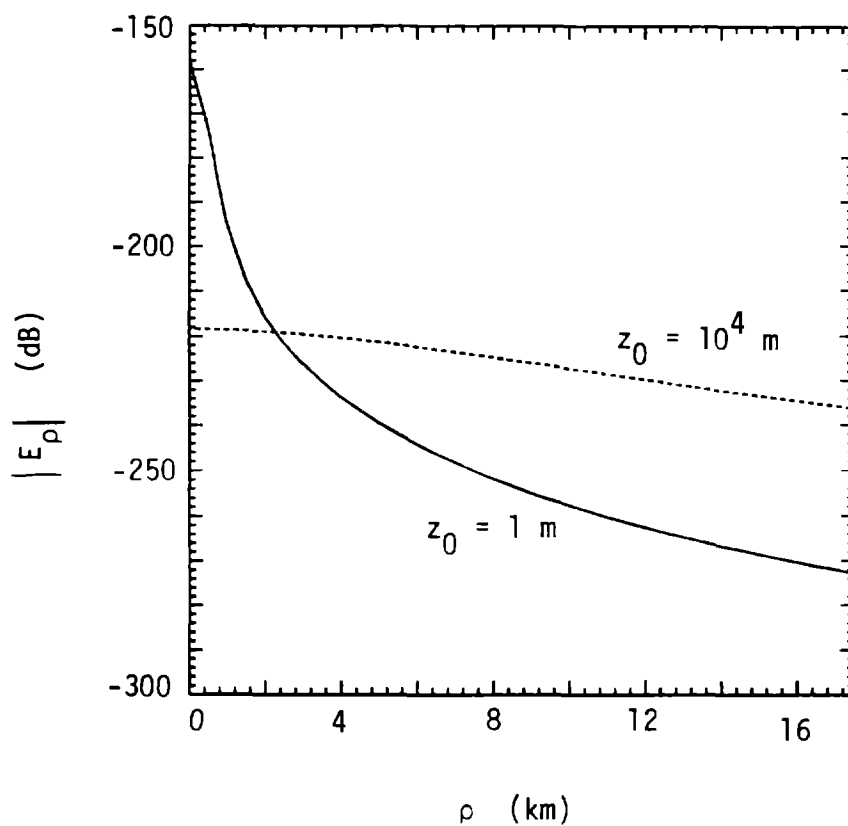


Figure 9. Electric field in air over the center of an insulated horizontal dipole antenna. The dipole is at a depth of 762 m (2500 ft) in a ground with conductivity of 0.01 S/m. The field is shown at heights of 1 m and 10 km above the interface as the dipole length is varied up to 32 km (20 mi). Frequency is 1 kHz.

strength at the center of the dipole is plotted as the length of the dipole is varied up to 32 km (20 mi) for receiver heights of 1 m and 10 km above the earth.

These results can be understood by examining changes in the field of a buried point source as the receiver location is displaced laterally from directly over the source. As shown in Fig. 10, the field at a height of 1 m is sharply peaked over the point source, while at 10^4 m, the field is more distributed. Thus, since the field radiates mainly from the ends of the dipole, the strength at the center at a height of 1 m decreases for lengths greater than about 1.6 km (1 mi). The increase in field strengths up to a length of about 26 km (16 mi) at 10 km height is due to improved efficiency. As the length is increased, less power is dissipated in the ground in the vicinity of the dipole. If the length was increased beyond 32 km (20 mi), the field would eventually decrease since the field from different parts of the distributed source would arrive out of phase at the receiver.

Input impedance of the buried insulated dipole is shown in Fig. 11. The large reactance would make the antenna very difficult to excite for lengths less than several miles. A more reasonable input impedance is obtained if the ends of the insulated dipole are grounded. The current distribution and input impedance with grounded ends can be obtained as a simple modification of the equations used in Sec. 2.3.

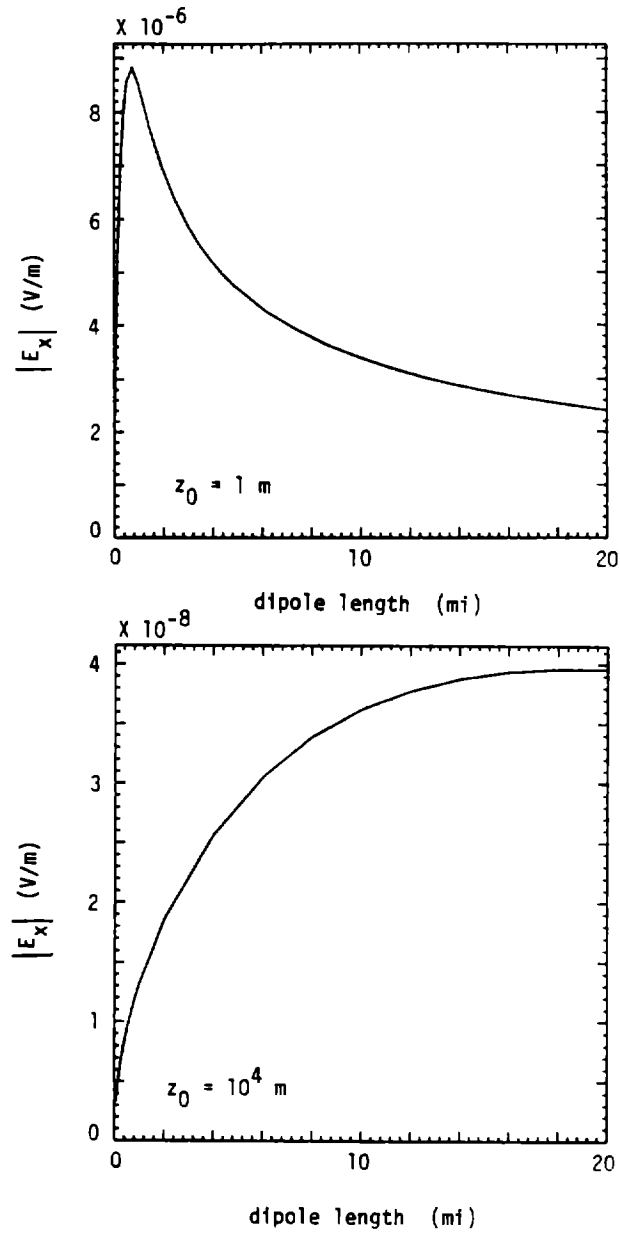


Figure 10. Field over a horizontal point-dipole source. The sharp peak over the source for a receiver height of 1 m explains the decrease in field strength as the length of a finite dipole is increased.

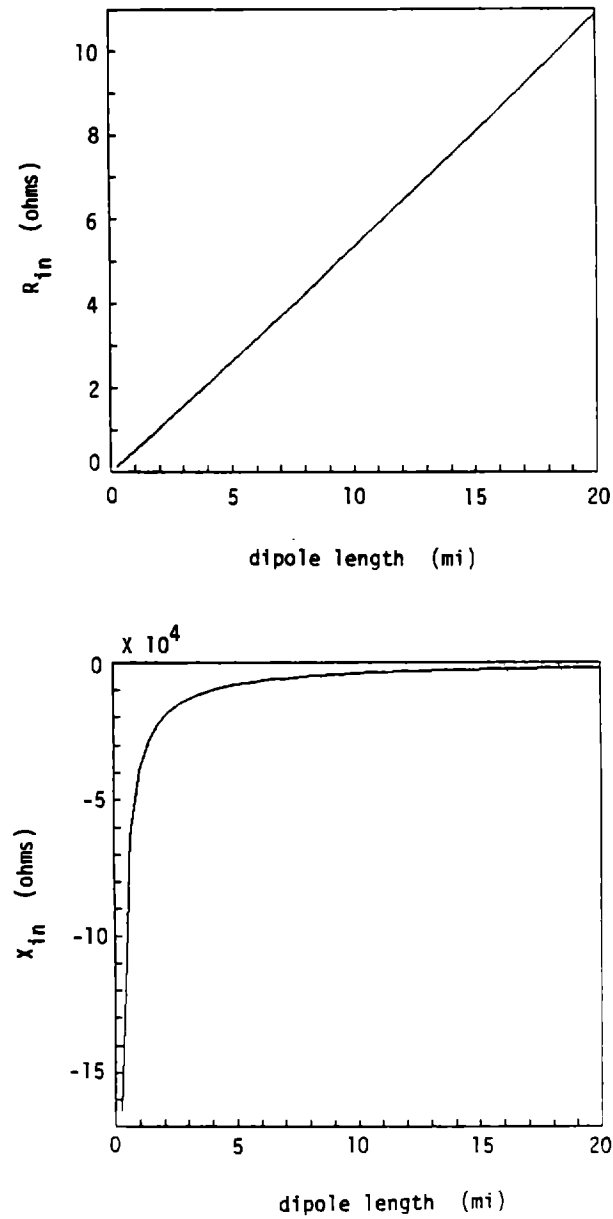


Figure 11. Input resistance and reactance of an insulated antenna with open ends as the length is increased.

2.4.3. Summary of Numerical Modeling

Electric and magnetic field calculations for a point source buried in a half space provide an initial estimate for the transmission quality of through-the-Earth communication at selected frequencies. Additional sophistication is provided by including a stratified model of the Earth. Here, changes in rock type and water saturation can be accounted for by changes in conductivity σ and dielectric constant ϵ . To see if practical antenna and power requirements are applicable to a particular transmitter arrangement, one needs to consider a finite-length antenna. Besides considering the finite-current distribution, the effects of insulation on the antenna must be considered. Calculation of fields due to a buried, insulated, finite-length, electric dipole incorporates our numerical solution for a point source in a half-space (Lytle and Lager, 1974) with the approximate current distribution (Guy and Hasserjian, 1963; King, 1981) for the insulated wire. Use of the finite current distribution allows one to estimate the efficiency of the antenna.

For the specific examples studied, through-the-Earth communication looks promising for frequencies up to a few kHz for earth conductivities up to 10^{-2} S/m and for depths up to 762 m (2500 ft). Further consideration is needed to evaluate signal/noise requirements and options for practical antenna design. Also, it is desirable to combine the stratified model capability with the finite length antenna code so that specific geological sequences can be evaluated for practical antenna lengths.

3. EXPERIMENTAL RESULTS

3.1. GOALS OF THE EXPERIMENTAL PROGRAM

Our experimental program had four major goals. First, we wanted to determine the in situ electrical attenuation characteristics for ELF-VLF (200 Hz-30 kHz) frequencies in representative rock media. At these frequencies, this amounts to determining the electrical conductivity of the rock media. Second, we wished to test the utility of various instruments and antennas for through-the-Earth transmission. Third, we wanted to evaluate the utility of our computer codes and associated assumptions. Finally, we wished to obtain an estimate of the channel capacity for rock media, dominated by limestone formations.

To realize the first goal, some care is necessary in the design and execution of the experiments to ensure that the signals we measure are the result of transmission through the rock instead of through some alternate (sneak) path or due to electromagnetic interference (EMI).

To help distinguish the true signal from sneak-through or EMI, we measured both signal magnitude and phase. Having two independent measurements instead of one provides additional information for recognizing the desired signal. We tried to eliminate sneak paths by using fiber-optic links between stations for the voice and phase reference signals, thus eliminating direct electrical connection between the transmitter and receiver stations.

3.2. YOSEMITE EXPERIMENT

3.2.1. Location and Site Description

A set of experiments was conducted between the subsurface and surface using a side drift located off the Wawona Tunnel in Yosemite National Park. The site was in granite with a variable overburden thickness of about 61 m (200 ft) for locations directly over the drift. Although the side drift did not contain appreciable metal, the main tunnel did contain electrical cables. This site provided a testing ground for our equipment and for our method for determining the EM propagation path.

3.2.2. Summary of Experiments at Yosemite

A transmitting antenna, either a horizontal electric dipole or horizontal loop, was placed in the drift, and various electric and magnetic receiving antennas were located above the drift. A fiber-optic link was made between the transmitter and the surface receivers to provide a reference for phase measurements. Most transmissions were made in the 200 Hz-20 kHz range. However, additional transmissions were made up to 225 kHz using an inductively loaded dipole, which was field tested for the first time at this site.

Successful transmission was easily achieved up to 225 kHz. However, due to the expected small change in phase for this short transmission distance and the large uncertainty in the phase measurements, it was difficult to determine whether the principal transmission was through-the-Earth or through some reradiated path as could occur along the power cables in the tunnel. If one assumes that transmission was predominantly through-the-Earth for frequencies below 3 kHz, then the gross conductivity is of the order of 10^{-3} S/m. These

experiments highlighted the need for better design of our phase measuring system. Modifications were made before deploying the equipment in the later experiments in Pennsylvania.

3.3. LAKE LYNN LABORATORY EXPERIMENTS

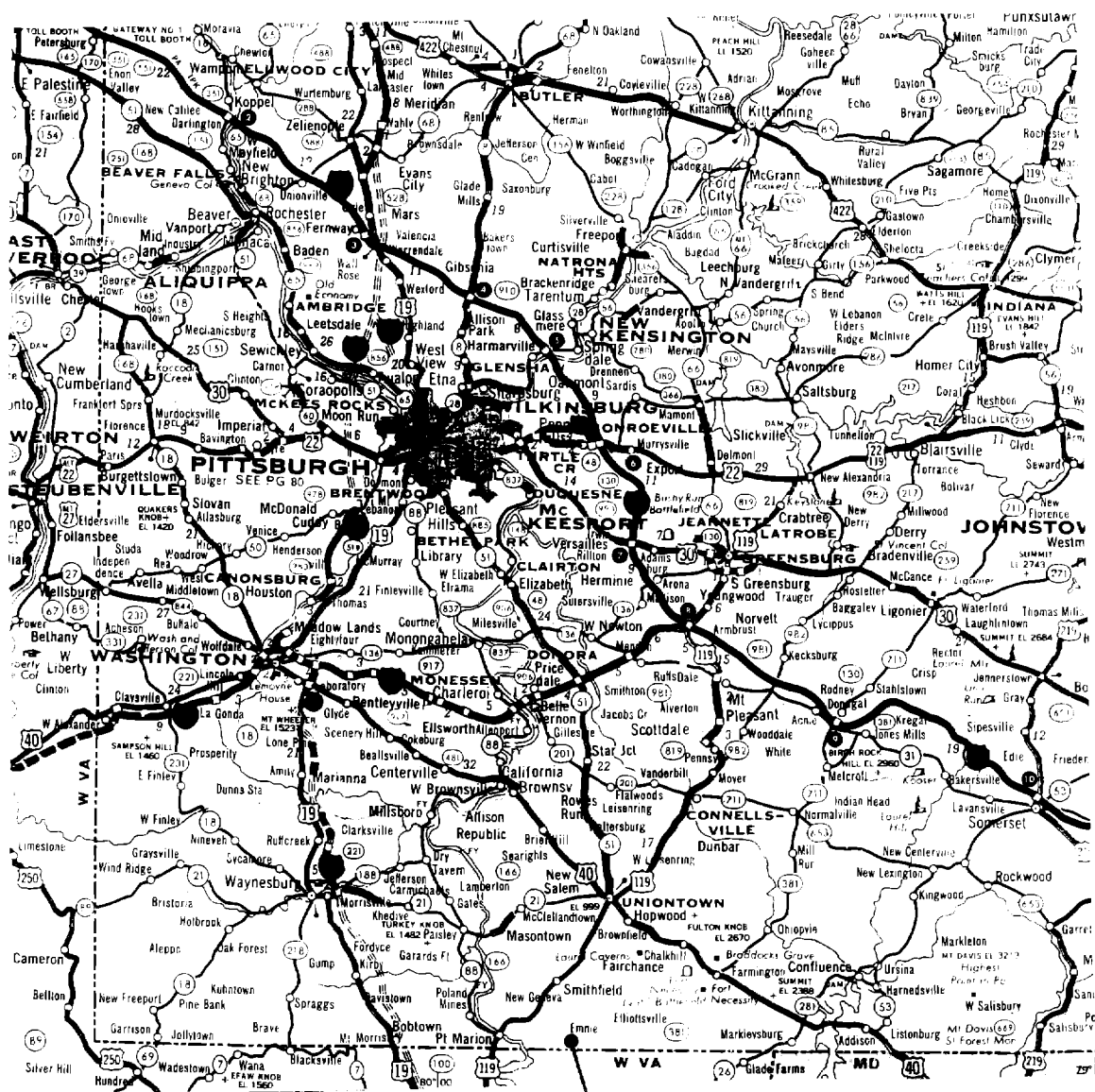
3.3.1. Location and Site Description

Lake Lynn Laboratory (LLL), formerly a limestone mine but now used as a multipurpose mining research laboratory by the U.S. Bureau of Mines, is located approximately 14 mi south of Uniontown, Pennsylvania, near the West Virginia border (see Fig. 12). Our experiments were located in the new workings at LLL, located under cover ranging from 55 to 95 m (180 to 310 ft) in thickness. The geology is dominated by the Greenbrier limestone formation, a relatively homogeneous formation consisting of hard, massive limestones and shales. Plan views are shown in Figs. 13a and 13b.

3.3.2. Summary of Experiments at LLL

We performed three general types of experiments at LLL. In the first, we transmitted from C to D drift (Fig. 13a) by the shortest possible path, about 152 m (500 ft). Secondly, we transmitted from C to D drift in a skewed fashion, thus increasing the transmission path to about 238 m (780 ft). In both cases, our transmissions did not cross the layered structure. Finally, we transmitted between the surface and D drift, a distance of about 101 m (330 ft). Here, of course, our transmissions crossed the layering.

We had hoped that each of these three types of experiments would provide us with unique information. We expected that the direct transmission from C



Lake Lynn Lab

Figure 12. Location of the Lake Lynn Laboratory (LLL).

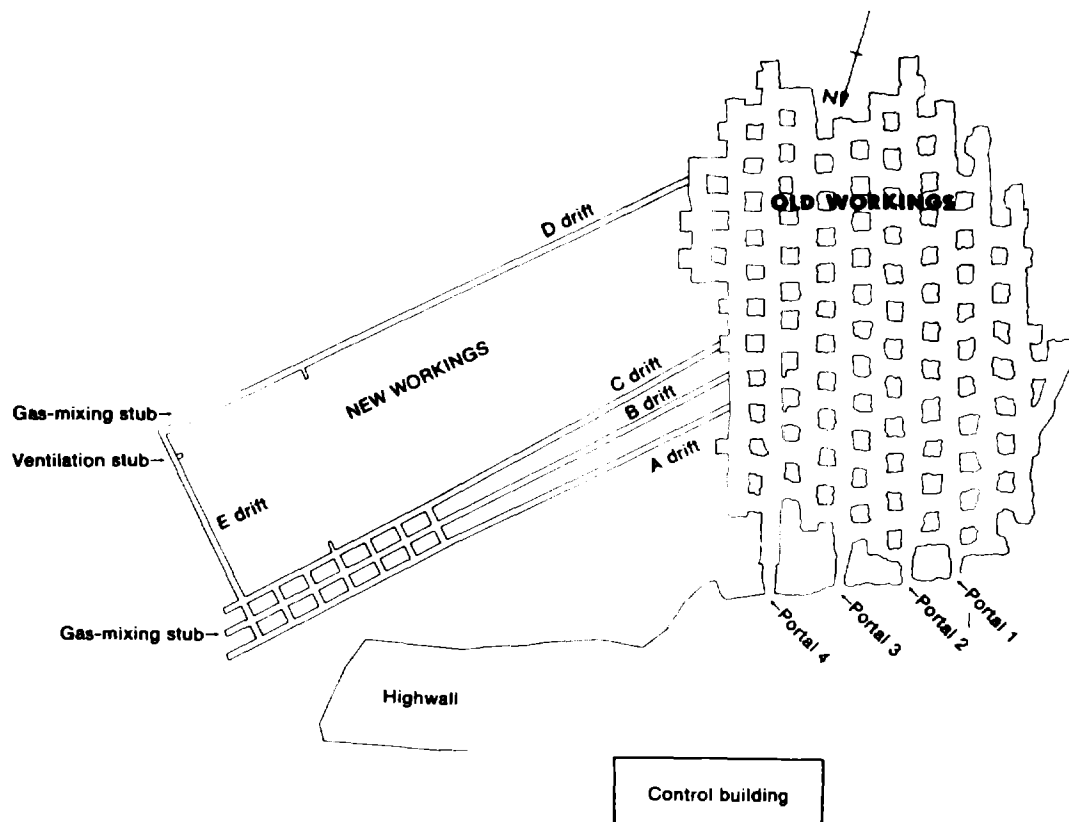


Figure 13a. Plan view of the underground workings at LLL.

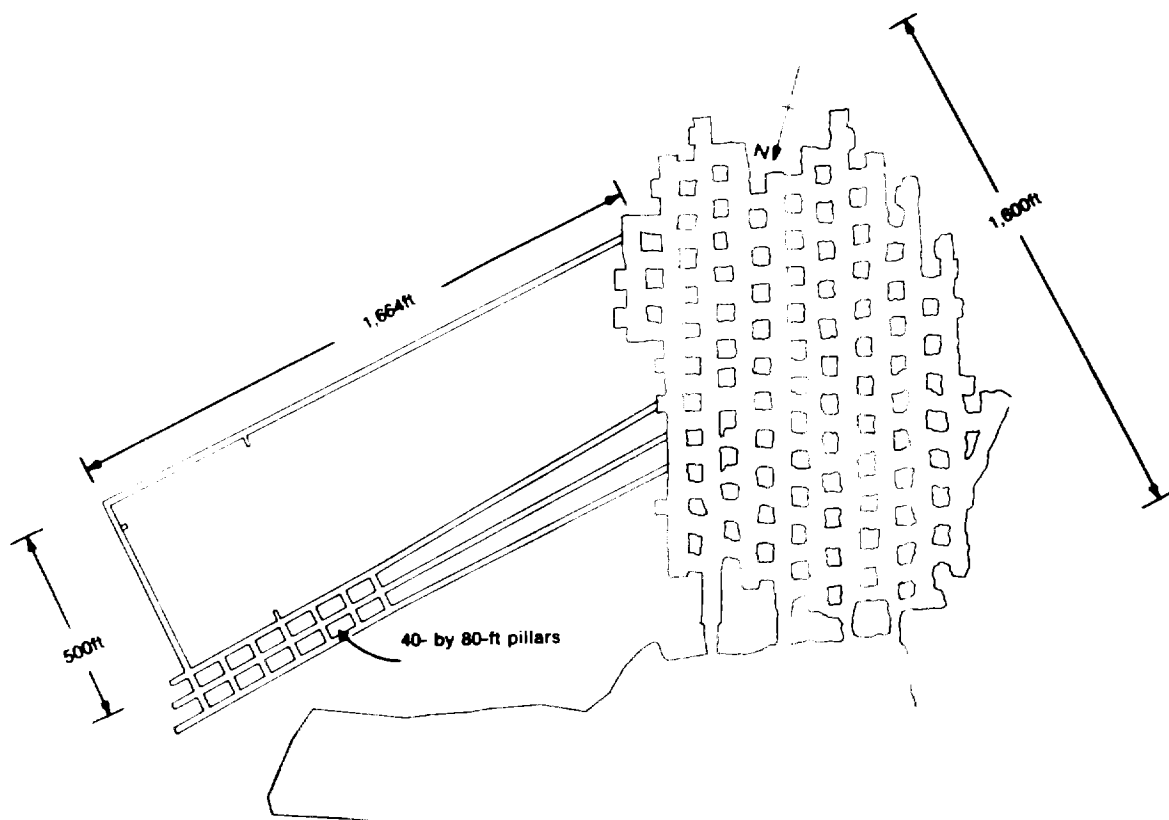


Figure 13b. Approximate dimensions of the underground workings at LLL.

to D drift would tell us about the electrical conductivity at that depth without the complication of layering. The skewed-transmission experiment was designed to help separate the desired through-the-rock path from signals that had traveled through other sneak paths. We expected that the surface-to-D-drift experiment would tell us about the conductivity of the upper layers. Finally, all of these experiments allowed us to evaluate our antennas and instrumentation.

3.3.3. Experimental Results and Discussion

Our results are presented according to the scheme above rather than chronologically. In some cases we shall present only brief descriptions of experiments along with overall conclusions. Most often we present the experimental data and computer calculations in the form of plots.

Every field site has a unique set of sources for noise and interference. As a consequence, we always made a quick survey of these sources before beginning our measurements. We set up our receiver probes and electronics as if we were making an actual measurement, but then, by using a spectrum analyzer that covered the frequency band of interest, we monitored the received signals with the transmitter turned off. Those frequency values for which there was a significant source of interference were recorded, and care was taken to avoid those values during our measurements. It should be no surprise that harmonics of the 60-Hz powerline frequency are a common source of interference, but there are others as well.

We present the results of the C-to-D-drift transmission experiments first. The setup is shown schematically in Fig. 14. A 64-in-square

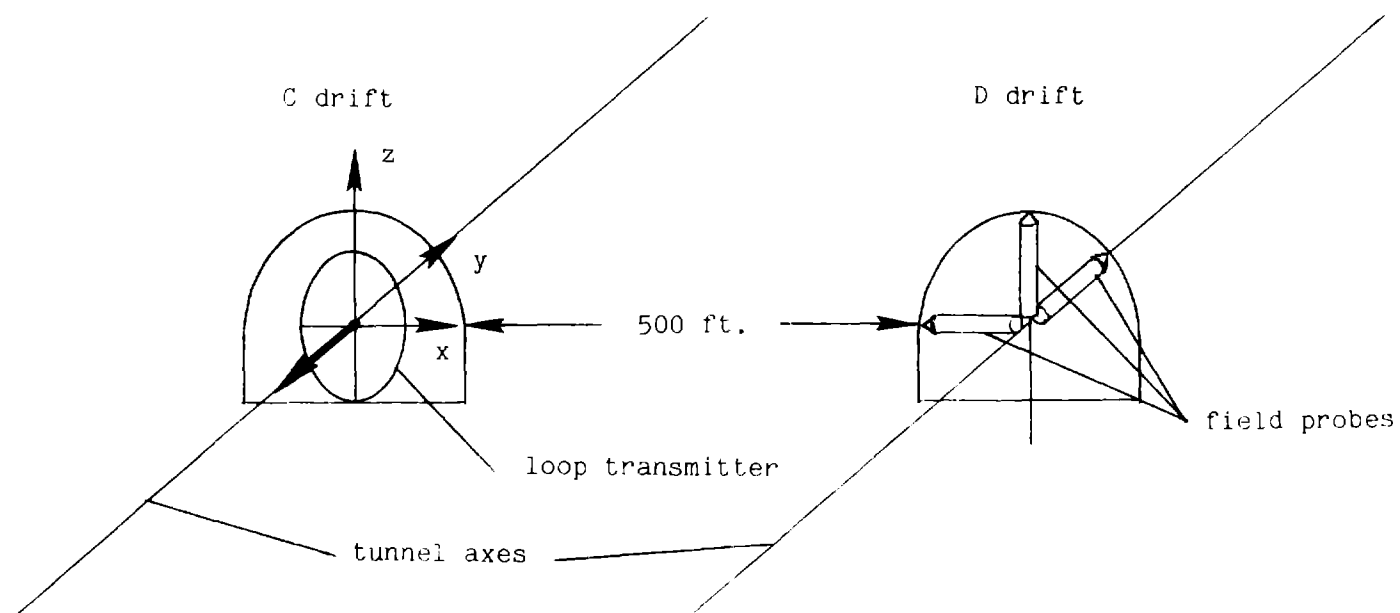


Figure 14. Layout for C-to-D drift transmission experiments at LLL. See also Fig. 19a.

transmitter loop consisting of 4 turns of wire was aligned with its axis along the tunnel (y axis). This loop was excited with a GR 1308 oscillator/amplifier at low frequencies (200 Hz-20 kHz) or an HP-240 oscillator/ENI 1140A amplifier in the frequency range 10 kHz-100 kHz. We used Electro Magnetic Surveys-calibrated magnetic field probes in the low-frequency regime. For the high frequencies, we used a 64-in-square loop of 21 turns, or an active electric field monopole probe.

In the low frequency range, the receiving electronics consisted of an HP-3582 spectrum analyzer. In the high frequency range, we used an HP-3585 spectrum analyzer or a PAR 214 lock-in amplifier.

In the first set of experiments, we measured the x, y, and z components of the magnetic field in D drift. When possible, we measured both the magnitude and phase of the received signal. To facilitate the phase measurements, we used a nonconducting fiber-optic reference link.

Figure 15a shows the magnitude of the magnetic field components over the frequency range 200 Hz-20 kHz. We have also shown values of the y component calculated from our computer codes for rock conductivities of 10^{-3} , 3×10^{-3} , and 10^{-2} S/m. Theoretically, the x and z components of the field are zero; hence those components are missing from the computer results. The values are plotted in decibels relative to 1 A/m of magnetic field.

Comparison of the three computer-generated curves with the experimental data for H_y show good agreement below 1 kHz. The value of H_y is also fairly independent of electrical conductivity below 1 kHz. Above 1 kHz, the experimental values for H_y are much greater (10 dB in the worst case) than the computed values. Changing the value of conductivity in the computer calculations will not make the results agree above 1 kHz.

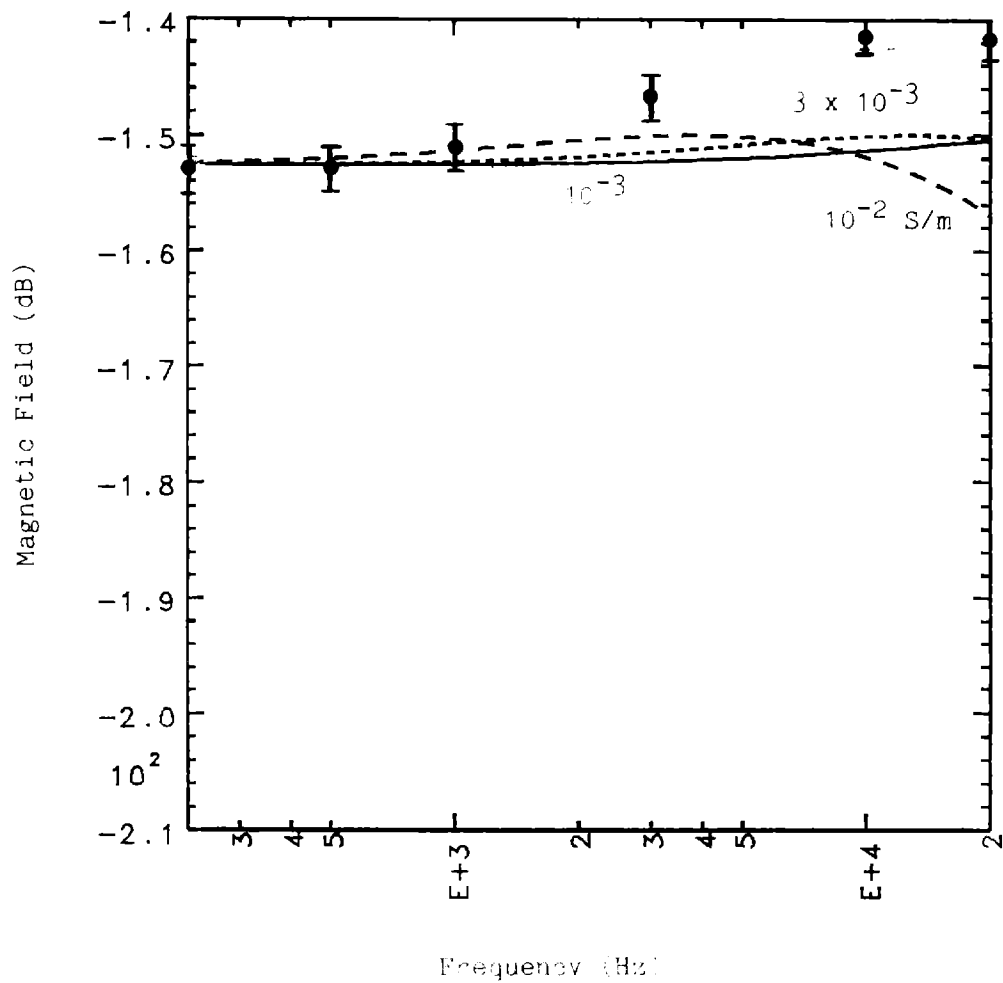


Figure 15a. Normalized magnetic field, H_y , at the receiver in D drift for direct transmission from C drift (dots show experimental values). Also shown are computer calculations for conductivities of 10^{-3} , 3×10^{-3} , and 10^{-2} S/m.

Figure 15b shows the measured x and z components of the field. Both components peak at 3 kHz, with the z component predominating. Computer calculations show that these field components should not be present even if one allows for the effects of varying conductivity, the presence of the air-earth interface 100 m above, or geologic layering.

It is possible that these nonzero values for the x and z components of the field are due, in part, to misalignment between transmitter and receiver probes. Another possible mechanism for this behavior is the capacitive coupling of electric fields from our loop transmitter onto the conductors present in C drift (e.g., power distribution system, electrical cables, water lines, gas lines, reinforcing screen) and back onto our receiver probes and cables in D drift. Our simple modeling shows that this type of coupling mechanism can produce sneak signals equal to or greater than those propagating through the direct path. In addition, this type of coupling mechanism would produce the sort of peaked response that we observed.

Finally, it is possible that we measured magnetic fields that resulted from eddy currents circulating in the man-made conductors associated with the tunnel. The observed magnetic fields have two components: the primary field of the transmitter, and the scattered or secondary field produced by eddy currents in any conductors (natural or man-made) present. It is possible that the fields created by eddy currents in man-made conductors can overwhelm those produced by eddy currents in the rock. This problem can only be alleviated by working in an area where man-made conductors are absent.

For completeness, the phase of H_y is shown in Fig. 16 along with the computer plots for conductivities of 10^{-3} , 3×10^{-3} , and 10^{-2} S/m. Since the

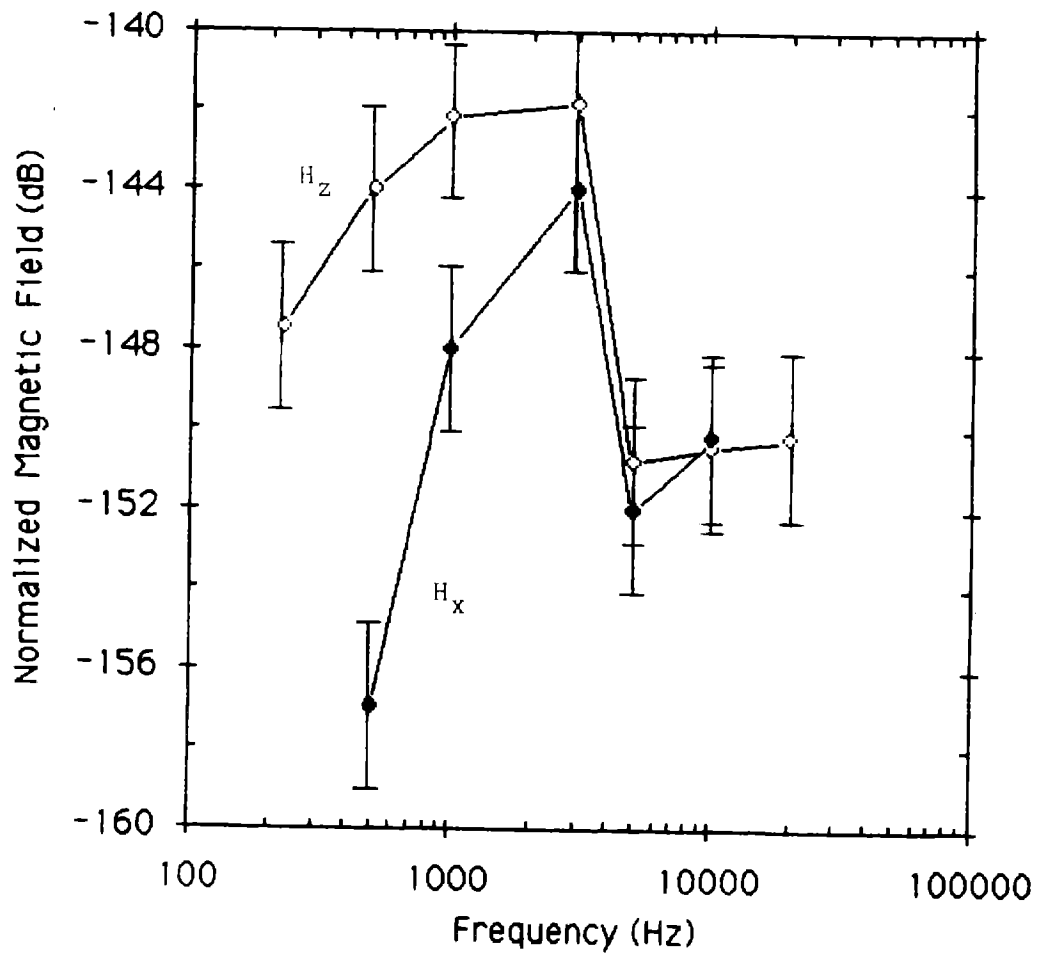


Figure 15b. Normalized magnetic fields, H_x and H_z , at the receiver in D drift.

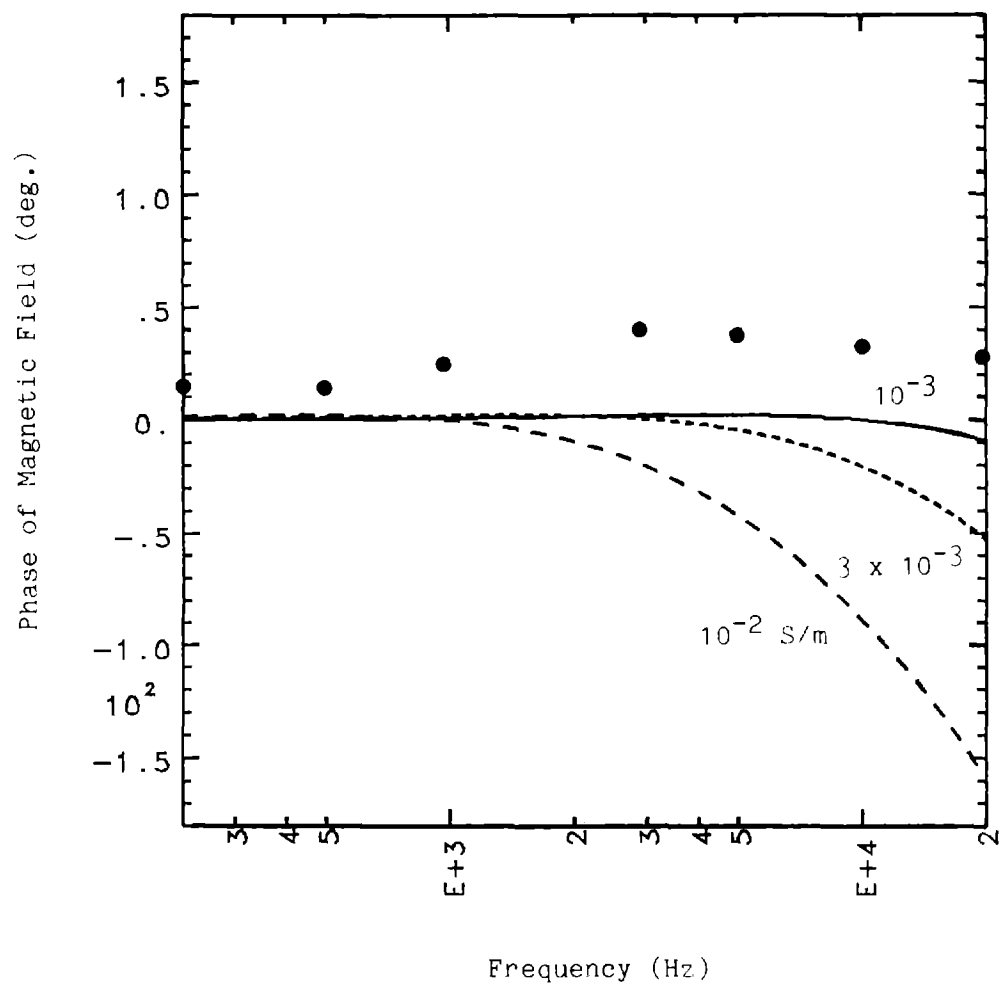


Figure 16. Phase of the magnetic field, H_y , for the experiment of Fig. 14.

uncertainty in our phase measurements is about $\pm 5^\circ$, the agreement below 1 kHz is good. Above 1 kHz the agreement deteriorates.

The results of our experiments to 100 kHz are shown in Figs. 17 and 18. In Fig. 17 we plot the values for H_y measured with the 64-in-square, 21-turn loop (10 kHz-100 kHz), along with the low-frequency data of Fig. 15. In the vicinity of 10 kHz, the two experimental curves disagree by about 2.6 dB. We have also shown values of H_y computed from Wait's analysis (1952) for a conductivity of 10^{-3} S/m. The good agreement between calculations and experimental data below 1 kHz, the increase in signal up to 50 kHz, and the peaking of the signal are all strong indicators that our measured values are dominated by capacitively coupled EMI for frequencies above 1 kHz.

The measured and computed values of phase of H_y are shown in Fig. 18. In the vicinity of 10 kHz, there is a 20° discrepancy between the experimental curves. Between 10 kHz and 100 kHz, the slopes of the measured and computed curves are quite different. We believe that this behavior is probably caused by capacitively coupled EMI.

We also made measurements of the x-component of the electric field for the C to D drift transmission experiments. These data also show the steady rise and peaking behavior in the neighborhood of 50 kHz observed with the magnetic field measurements. This is in contrast to our computer calculations and is believed to be the result of capacitively coupled EMI.

The skewed transmission experiment from C to D drift was designed to help identify possible sneak paths. Figures 19a and 19b show the top view of the layout. In Fig. 19a, the direct path is 152 m (500 ft) in length, and the sneak path is about 476 m (1560 ft). In Fig. 19b, the direct path is 238 m

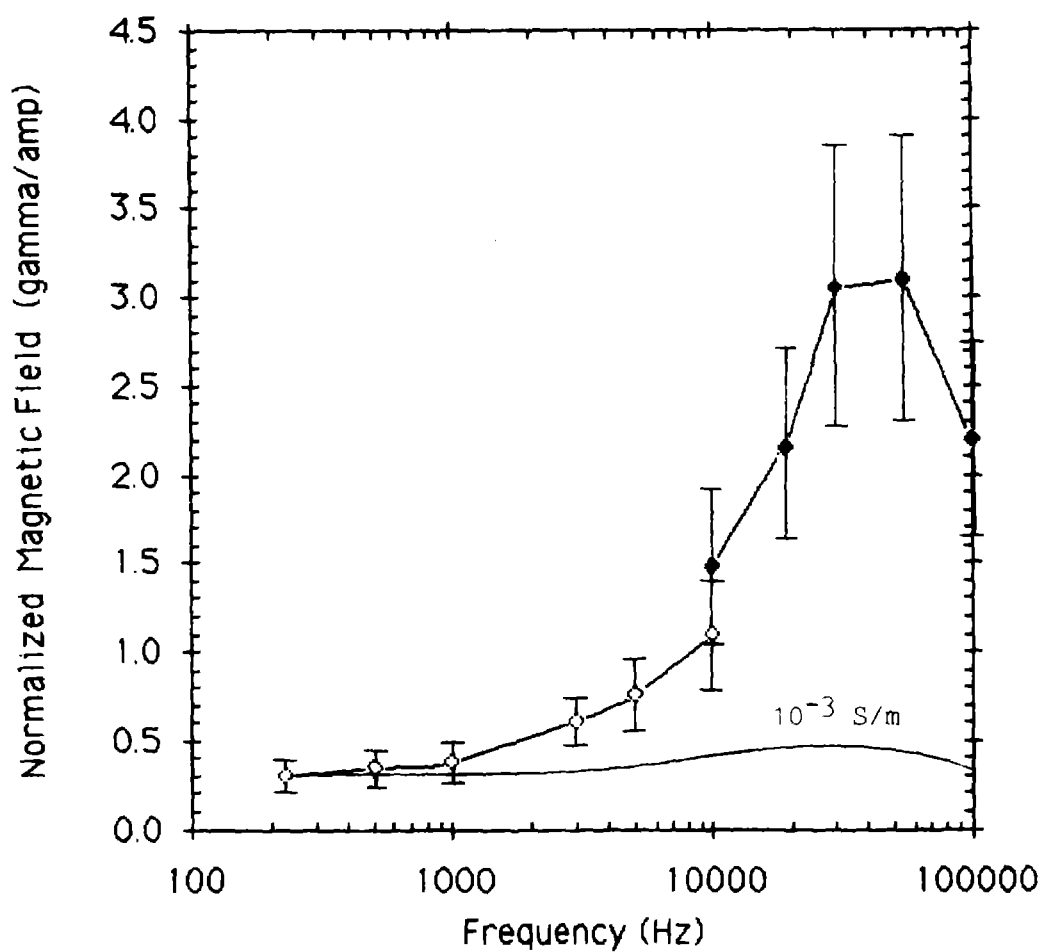


Figure 17. Normalized magnetic field, H_y , in D drift for the experiment of Fig. 14. We also show the curve computed according to Wait (1952) for a conductivity of 10^{-3} S/m.

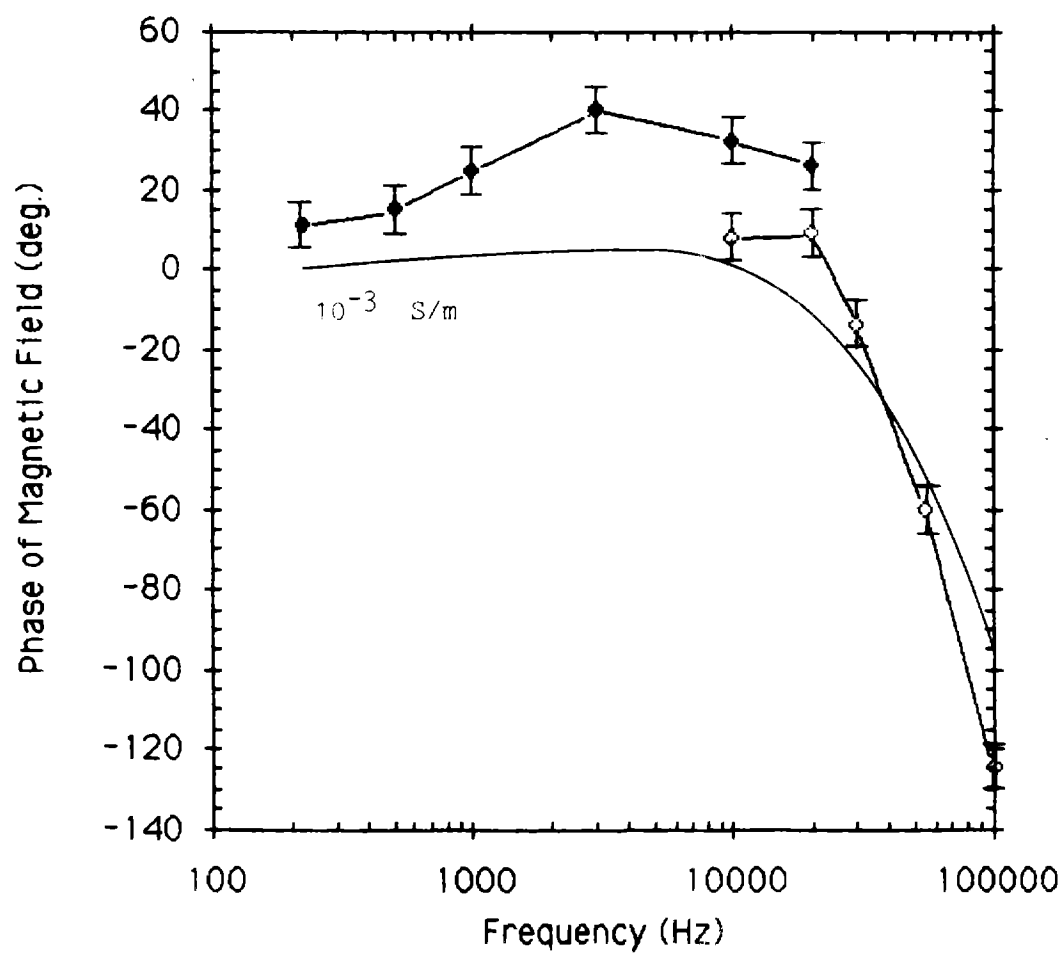


Figure 18. Phase of H_y in D drift for the experiment of Fig. 14. We also show the curve according to Wait for a conductivity of 10^{-3} S/m.

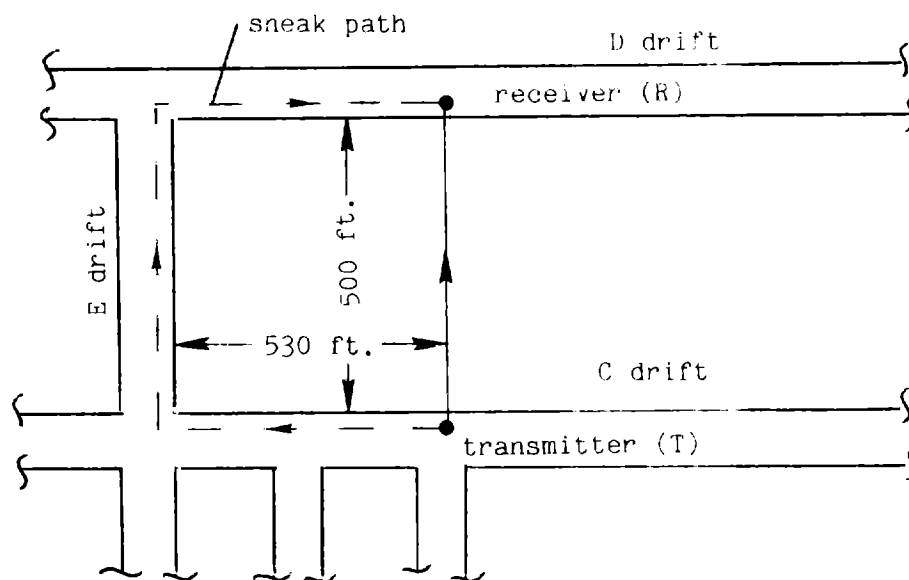


Figure 19a. Plan view of the direct transmission experiment from C to D drift. See also Fig. 14.

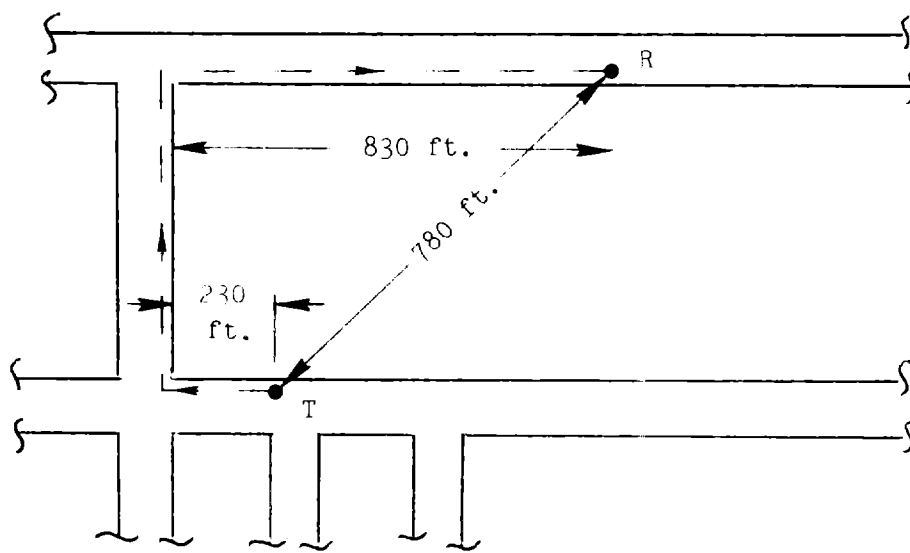


Figure 19b. Plan view of the skewed transmission experiment from C to D drift.

(780 ft), but the sneak path is still 476 m (1560 ft). The transmitter antenna is the 64-in-square, 4-turn loop with its axis oriented along y. We expect the direct signal to be greatly diminished in Fig. 19b because of the increased attenuation in the rock, while the sneak path should be about the same.

We show the results in Fig. 20. H_y was too weak to measure at the low frequencies but was measurable from 10 kHz-100 kHz. We were also able to measure a few values of H_z in the low frequency regime.

Note that the measured values of H_y increase monotonically with frequency between 10 kHz and 100 kHz. For contrast, we plot the curve computed from the model of Wait for a conductivity of 10^{-3} S/m. Note that this behavior is similar to that of the direct transmission experiments from C to D drift except that the overall signal levels are lower. No value of conductivity will bring the computed values of H_y into agreement with the measured values. The few values of H_z that we were able to measure show the same peak at 3 kHz, similar shape, and lower signal level than the direct C-to-D values.

Obviously, the increased path length has resulted in lower overall signal levels compared to the direct C-to-D transmissions. It would appear that the sneak path or EMI problem remains.

We attempted to transmit from D drift to the surface but failed because of significant EM interference. Instead, we decided that it made more sense to transmit from the surface to D drift instead since our receiving probes and electronics would be in a quieter environment.

The arrangement for the surface-to-D-drift experiments is shown in Fig. 21. We used a 100-ft-square transmitter loop on the surface, and our

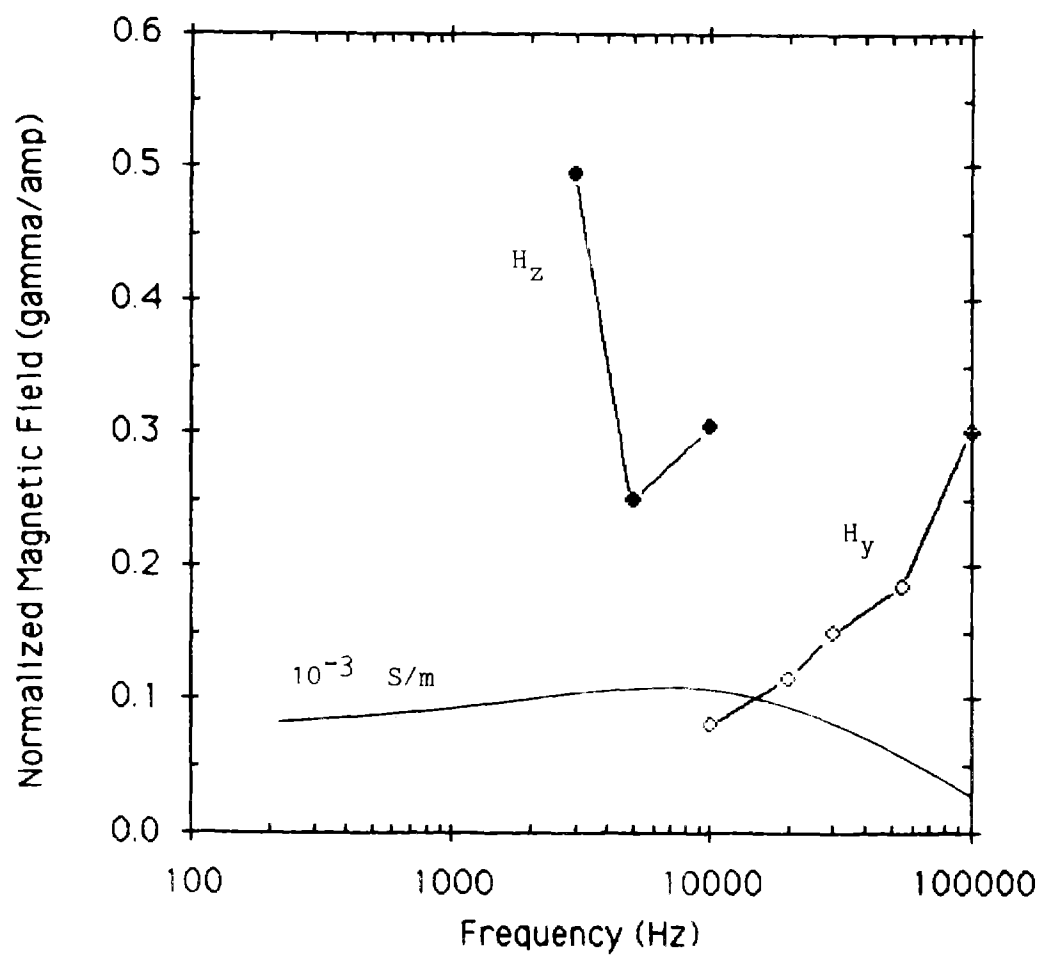


Figure 20. Normalized magnetic fields for C to D drift skewed transmission experiment of Fig. 19b.

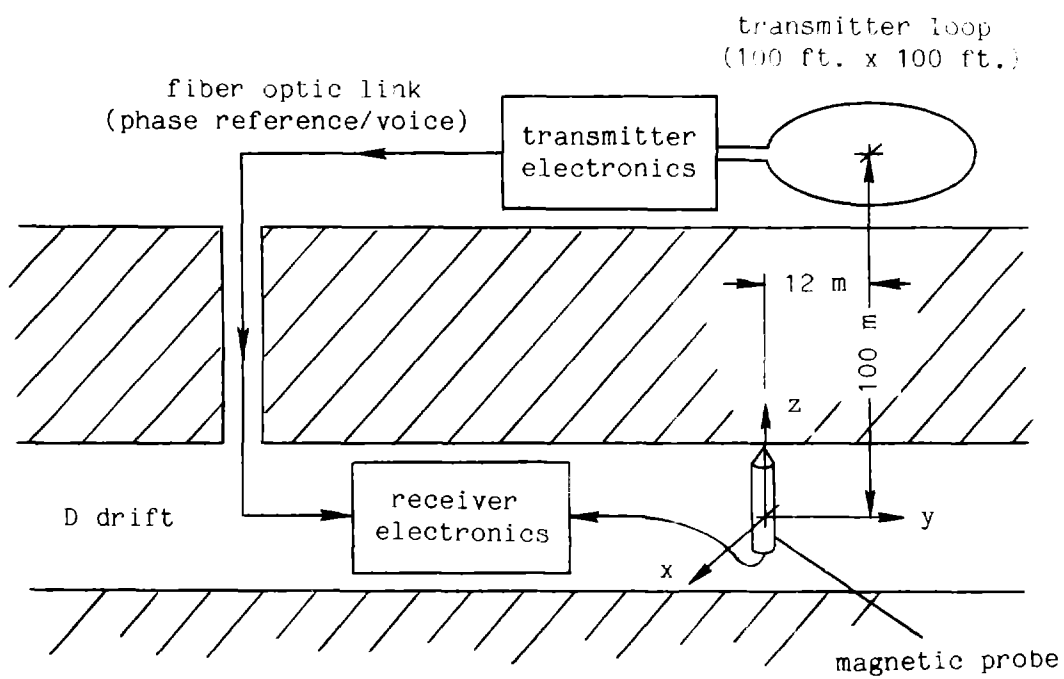


Figure 21. Cross-section of the layout for the surface-to-D-drift experiment.

calibrated magnetic receiver in D drift. The fiber optic reference link was brought down to D drift through a small vertical shaft.

We plot our results for the magnitude and phase of H_z in Figs. 22 and 23. The plotted values are in dB relative to a field of 1 A/m. In addition, we have shown computer calculations for conductivities of 10^{-2} , 2×10^{-2} , and 4×10^{-2} S/m. One can see that the agreement for the magnitude plots is 3 dB or better, and the agreement for the phase plots is 15° or better if we assume a conductivity of 2×10^{-2} S/m. Happily, the data do not appear to show any effects of sneak paths or EMI.

We also tried surface-to-D-drift transmissions using the 64-in-square, 21-turn loop with its axis oriented along y as the transmitter, but the received signal was overwhelmed by noise.

3.3.4. An Estimate of Channel Capacity at LLL

We shall now estimate the channel capacity for a medium like the limestone at LLL. The channel capacity depends on the signal-to-noise (S/N) behavior of the channel, the modulation scheme employed, and the noise characteristics. In Fig. 24 we show a plot of S/N ratio vs frequency for a hypothetical communications channel. At the lower frequencies, $1/f$ noise dominates, while at higher frequencies attenuation in the medium is dominant. A usable bandwidth can be defined by demanding that the S/N ratio exceed some threshold value. This condition is equivalent to requiring that the bit error rate be less than some chosen value. In Fig. 24, the bandwidth for $S/N = 40$ dB is about 30.7 kHz.

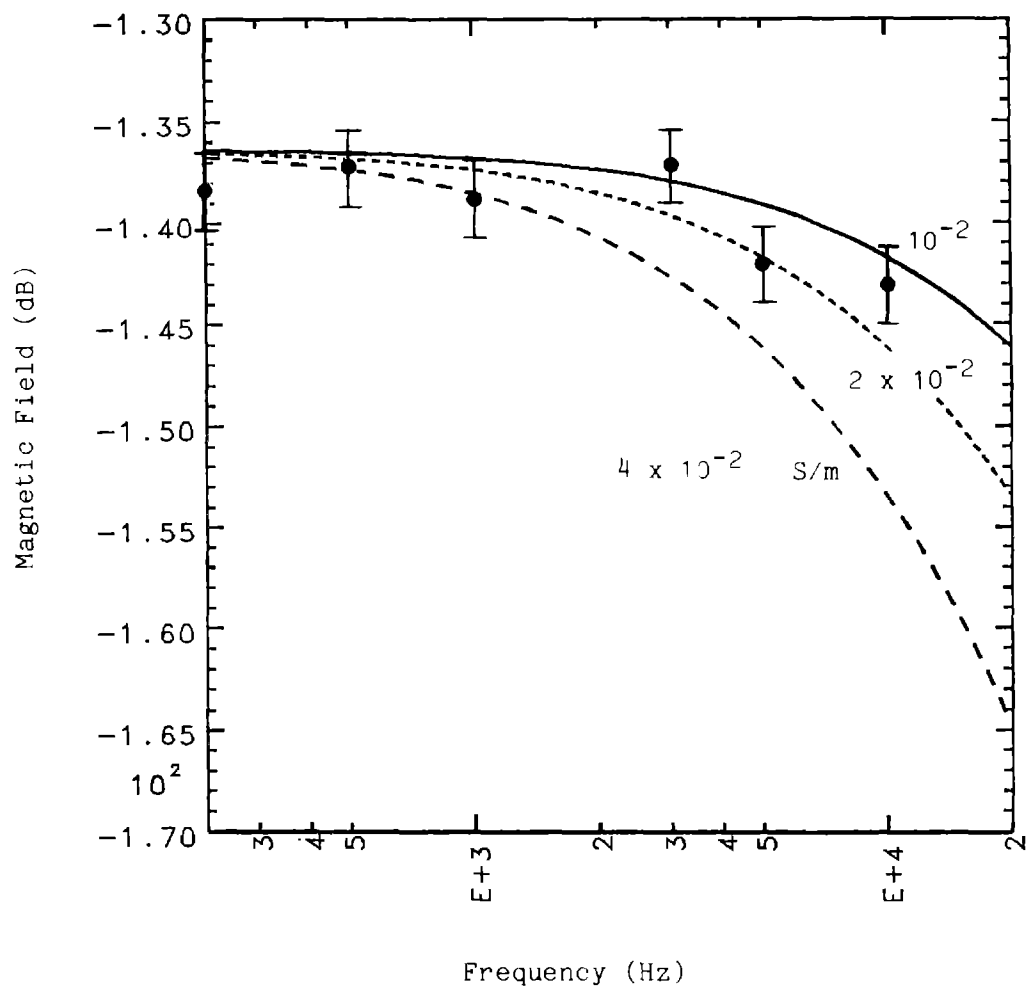


Figure 22. Normalized magnetic field, H_z , for the surface-to-D-drift experiment of Fig. 21 (dots). We also show computed curves for conductivities of 10^{-2} , 2×10^{-2} , and 4×10^{-2} S/m.

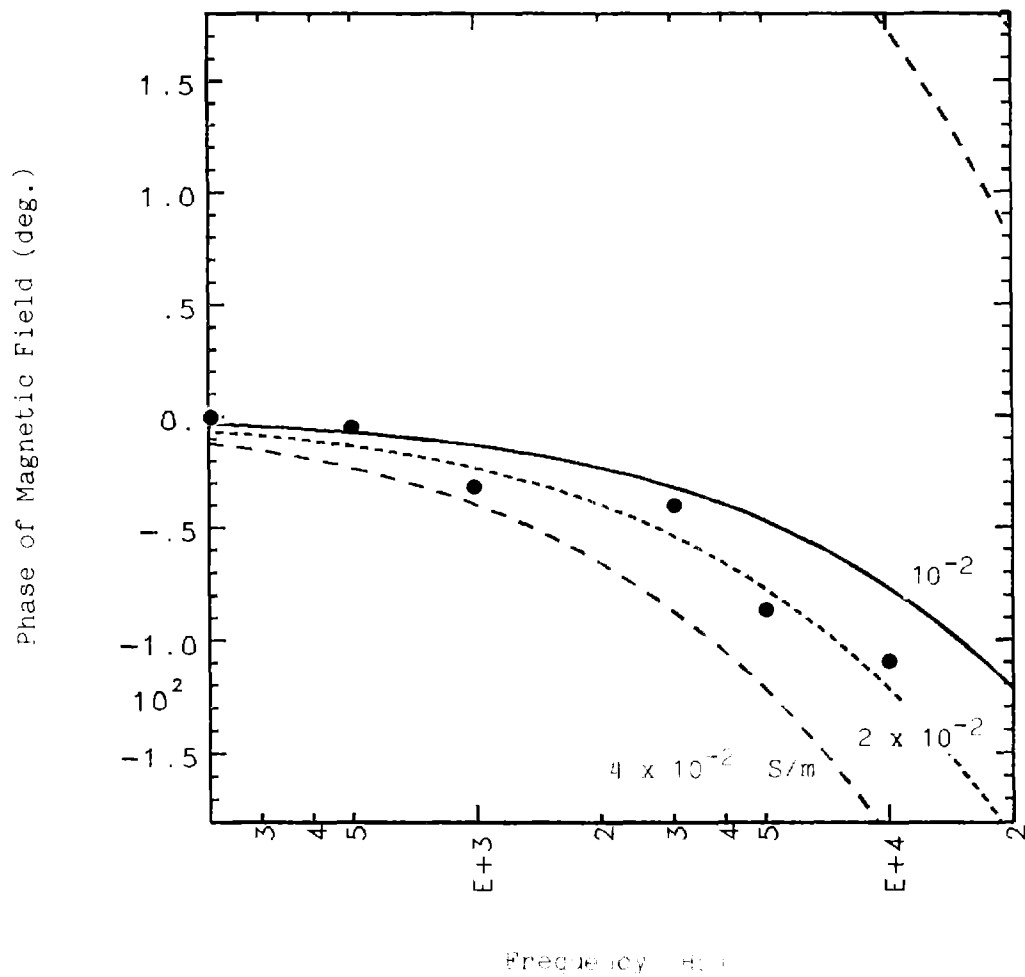


Figure 23. Phase of H_z for the experiment of Fig. 21 (dots). We also show computed curves for conductivities of 10^{-2} , 2×10^{-2} , and 4×10^{-2} S/m.

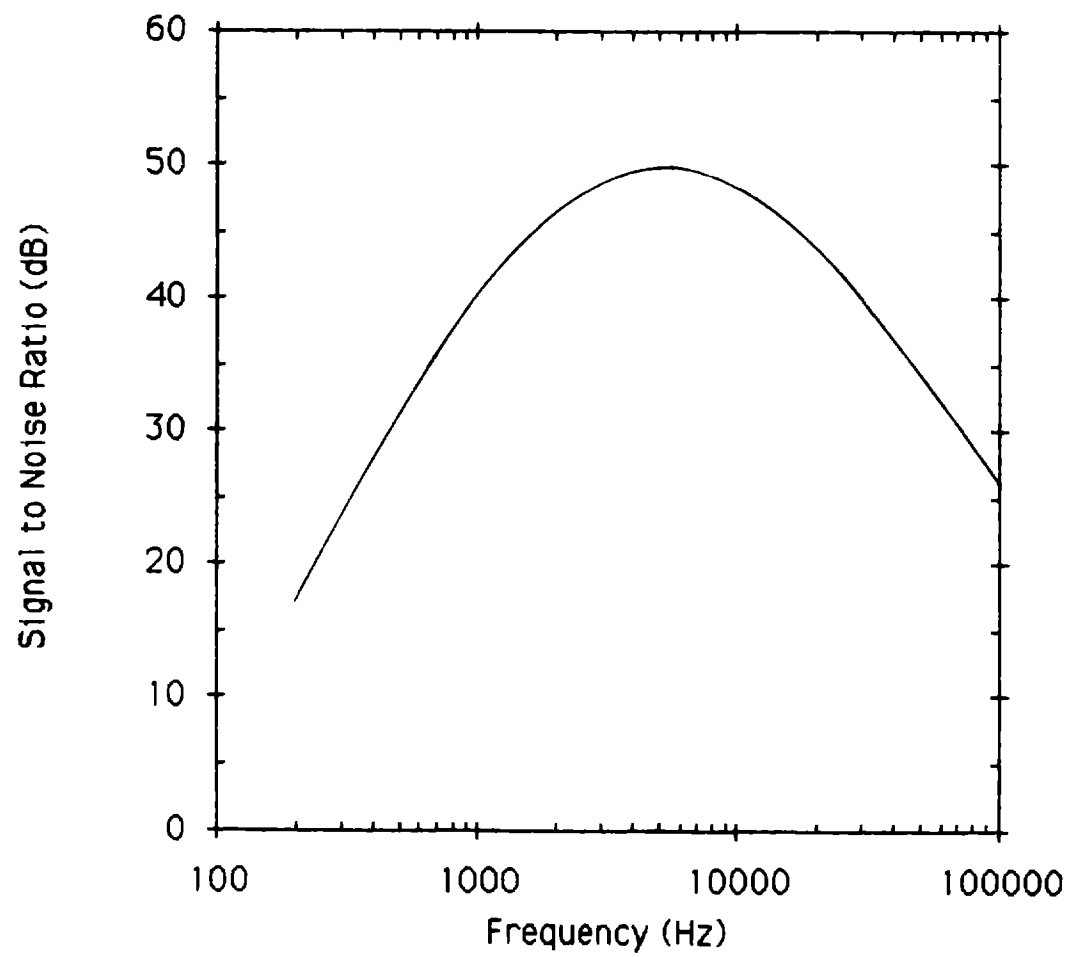


Figure 24. Signal-to-noise ratio (S/N) vs frequency for a hypothetical communications channel.

Figure 25 shows the ratio of channel capacity to bandwidth plotted vs S/N for a continuous channel with additive Gaussian white noise. Channel capacity does depend on both the type of modulation and the noise environment; however, our choice of a continuous channel model provides a universal means of comparing transmission properties. When S/N is 40 dB, this ratio is equal to 13.29. Thus, the capacity of our hypothetical channel is equal to 13.29 times the bandwidth or 408 kbits/s.

Figure 26 shows actual S/N ratio data for the surface-to-D-drift experiment discussed previously (upper plot). From this plot, one can see that $S/N \geq 23$ dB, and the useful bandwidth > 9.5 kHz. From Figure 25, the ratio of channel capacity to bandwidth is 7.5 when S/N is 23 dB. Thus, the theoretical channel capacity > 7.5 bit/s/Hz $\times 9.5$ kHz = 71.3 kbit/s.

We can now estimate the channel capacity at depths greater than 100 m by extrapolation of the S/N plots. To do this, we must first assume a model for the conductivity vs depth distribution at LLL. The model we have chosen is shown in Fig. 27. Note that the upper layer has a conductivity of 2×10^{-2} S/m as determined by our surface-to-D-drift transmissions. The conductivities of 10^{-2} and 10^{-3} S/m for the middle and bottom layers were picked as being realistic values for typical limestone media in this region. Assuming a constant value of 2×10^{-2} S/m from the surface to great depth will result in pessimistic values for channel capacity, and in any case, does not represent what is known about the geology at sites of this type.

We used our computer code to calculate values for the magnetic field at the receiver over the frequency range 200 Hz-20 kHz and at various distances D. At a given frequency, the received signal decreases with increasing D.

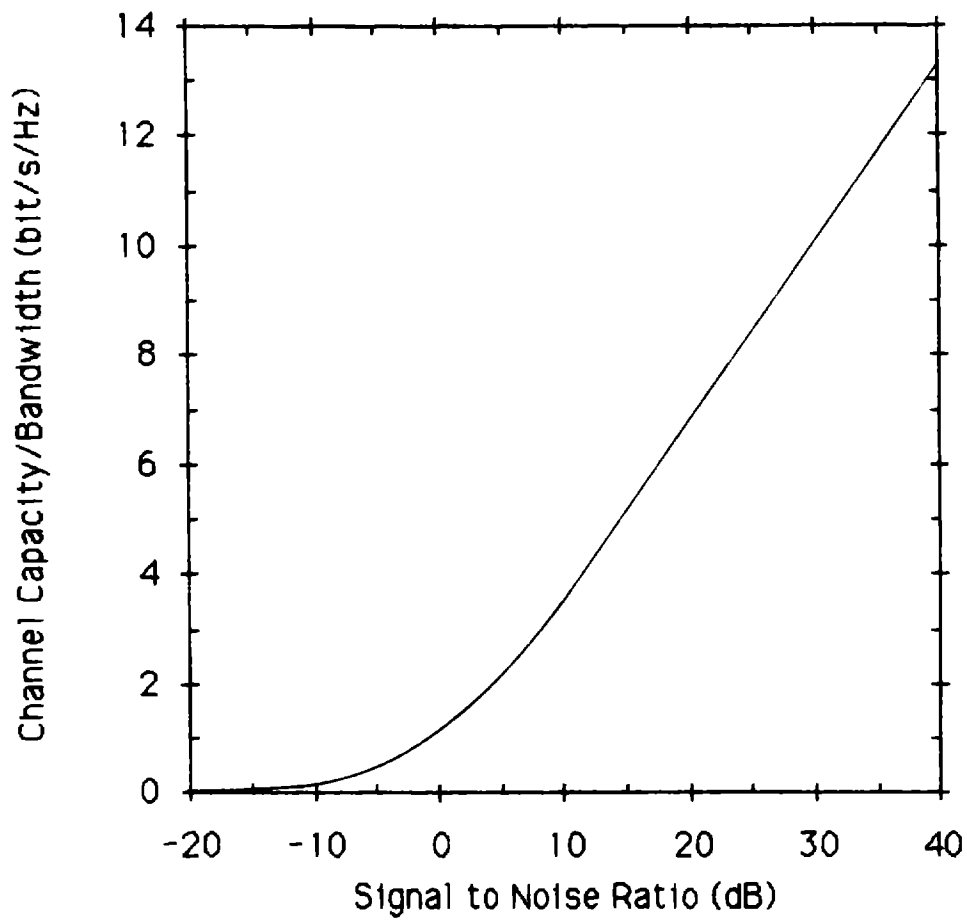


Figure 25. The ratio of theoretical channel capacity to bandwidth for a continuous channel with additive Gaussian white noise.

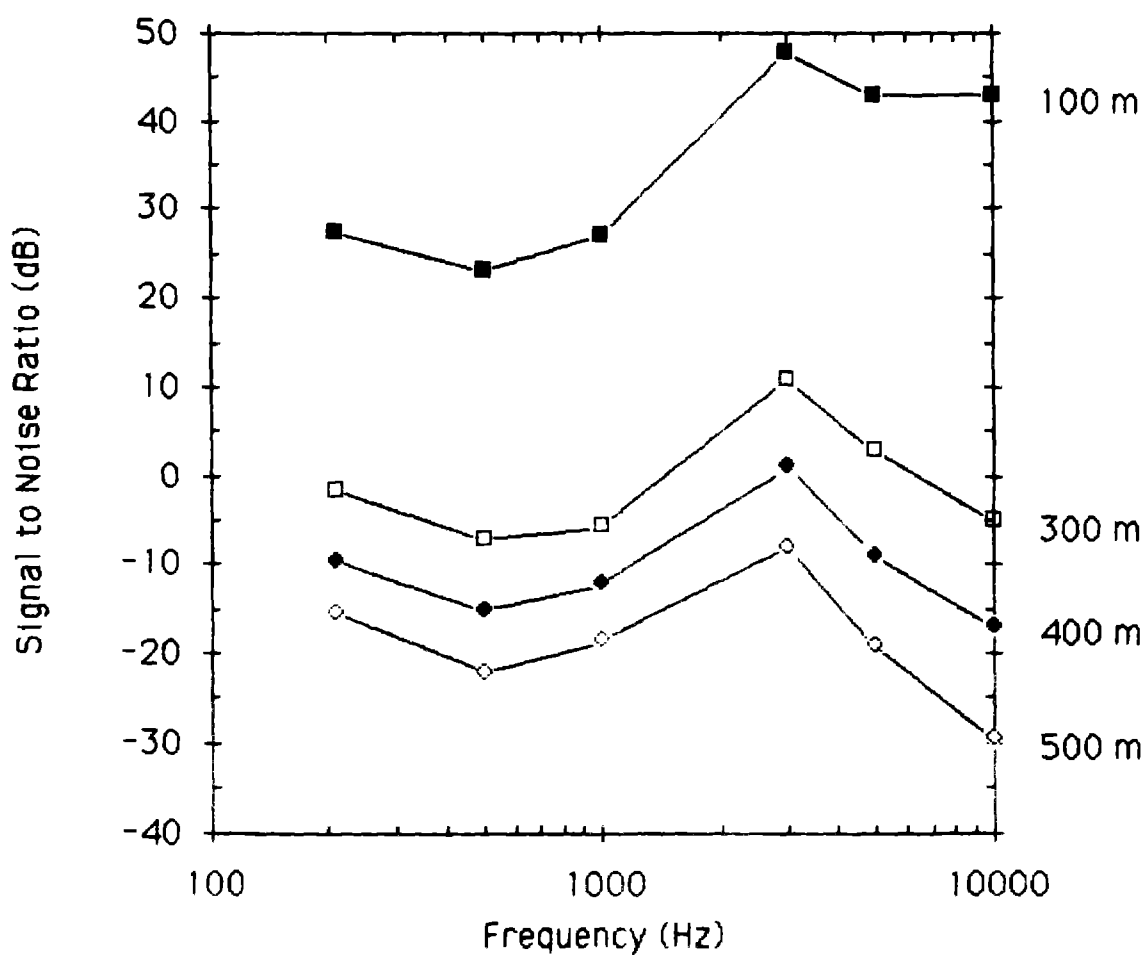


Figure 26. Actual S/N ratio data for surface-to-D-drift transmissions through 100 m of LLL limestone (top). Extrapolated S/N ratio for transmission through 300 m (984 ft), 400 m (1312 ft), and 500 m (1640 ft) of LLL limestone. It is assumed that the noise at a particular frequency is independent of depth.

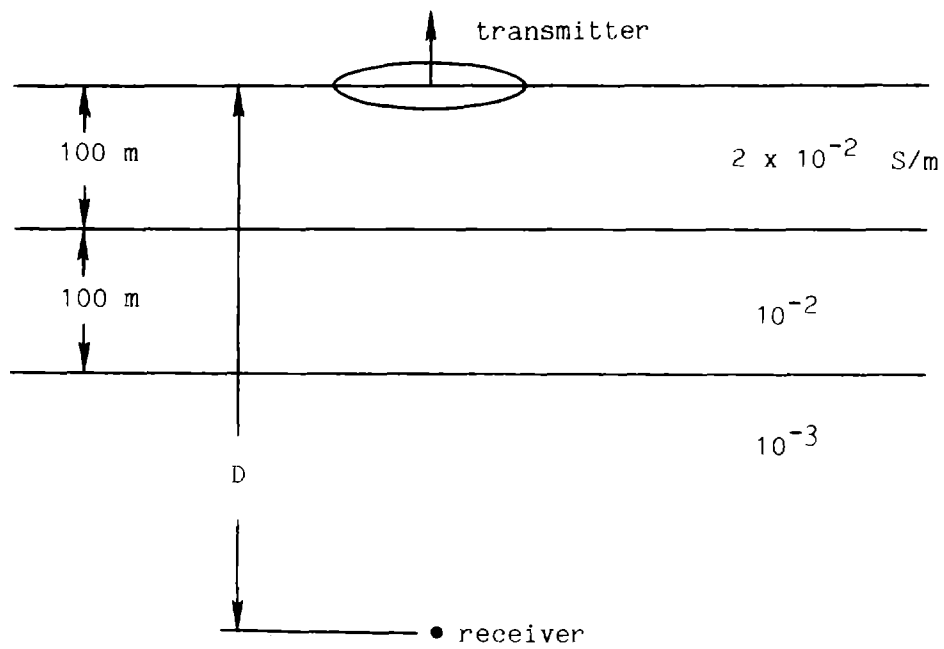


Figure 27. Layered conductivity model assumed for extrapolation of the S/N data from LLL.

Since we have experimental values for the signal level S and ratio S/N ratio at $D = 100$ m, we can extrapolate the expected signal level and signal to noise ratio to distances > 100 m. For example, at 200 Hz and 100 m depth, $S = 136$ dB and $S/N = 27.5$ dB. Computer calculations show that S decreases to ~ 165 dB at 300 m depth. Thus, the signal-to-noise ratio has decreased by 29 dB, resulting in a new signal to noise ratio of ~ 1.5 dB.

The remaining plots of Fig. 26 were derived in the above manner. Note that we have extrapolated S/N to depths of 300, 400, and 500 m. For $D > 500$ m, S/N is too low to be useful. We have made two assumptions in these calculations. They are: 1) the conductivity/depth model of Fig. 27 is accurate, and 2) the noise at a particular frequency is independent of depth.

Assumption 2 is incorrect to some extent because noise due to atmospheric sources will decrease with depth. However, noise due to thermal sources, which increases with transmission path, will increase with depth. The nature of the noise for subterranean transmission paths needs further definition.

We can now estimate the channel capacity for transmission to depths greater than 100 m using the results of Figs. 25 and 26. Examination of Fig. 26 shows that the maximum value of S/N has decreased to 11 dB at 300 m depth. In fact, if we require $S/N > 10$ dB, then the useful bandwidth is about 500 Hz. From Fig. 25, channel capacity/bandwidth = 3.46 when $S/N = 10$ dB. Thus, the maximum theoretical channel capacity is $3.46 \text{ bit/s} \cdot \text{Hz} \times 500 \text{ Hz} = 1.73 \text{ kbits/s}$. The results for the remainder of the curves are summarized in Table I.

Table I shows that transmissions beyond about 300 m with our present transmitter/receiver setup is not possible. An increase in signal power can,

Table I. Estimates of theoretical maximum channel capacity for transmission through 300 m, 400 m, and 500 m of LLL limestone.

<u>Depth (m)</u>	<u>S/N (dB)</u>	<u>Usable Bandwidth (Hz)</u>	<u>Channel Capacity (bit/s)</u>
100	>23	>9.8k	>71.3k
300	>10	500	1.73
400	>10	0	0
500	>10	0	0

however, help to improve the situation. In our experiments, we used about 2 A of current in our transmitter loop. With easily obtainable equipment, this current could be increased one-hundred-fold, or 20 dB. For this case, the S/N ratios of Fig. 26 can be increased by 20 dB. Table II shows the result of applying this procedure to the S/N data of Fig. 26. Note that the useful distance for transmission has been increased to > 500 m.

Transmission to depths greater than 500 m would require increased transmitter power or operation in less lossy media. Since most of the signal attenuation takes place in the upper layers, finding a site with lower electrical conductivity in the upper layers would greatly increase the transmission depth.

Obviously there is a penalty to be paid for transmission through thick layers. Channel capacity and S/N will be reduced (increased bit error rate) unless a forward error correction scheme is introduced.

3.3.5. Conclusions from Work at LLL

We shall now summarize what we learned from the LLL experiments. The in situ conductivity of the rock at LLL (average over the first 100 m) is about 2×10^{-2} S/m. This corresponds to attenuation constants of 0.024, 0.077, 0.24, and 0.77 dB/m at frequencies of 100 Hz, 1 kHz, 10 kHz, and 100 kHz, respectively.

Our measurement instrumentation worked reasonably well. It was helpful to have redundant instruments (2 spectrum analyzers and a lock-in amplifier) since we did have some trouble with both analyzers. The low-frequency spectrum analyzer is by far the easiest to use since it has many convenience

Table II. Estimates of theoretical maximum channel capacity for transmission through 300 m, 400 m, and 500 m of LLL limestone. We have assumed 20 dB higher transmitter power than that used to compute Table I.

<u>Depth (m)</u>	<u>S/N (dB)</u>	<u>Usable Bandwidth Hz</u>	<u>Channel Capacity (bit/s)</u>
100	>43	>9.5k	>136k
300	>13	9.5	42k
400	>10	4.1k	14.2k
500	>10	650	2.25k

features that the others do not have. Among these are signal averaging, dual channel capability, and the ability to measure phase directly. Unfortunately, it is limited to frequencies below 25 kHz. There are, however, other instruments available that can be used for the frequency range above 25 kHz. Two examples are the HP-3577A network analyzer and the HP-3562 spectrum analyzer.

Loop antennas worked very well in our experiments. They are easy to deploy and modify. In addition, they are easy to drive with our power amplifiers. Our helical dipole antenna, which is more compatible with deployment in drifts or boreholes, was difficult to drive above 20 kHz. We shall need to work on this problem.

Our drift-to-drift experiments at LLL were dominated by the effects of EMI. In the future, we shall need to implement new methods of diagnosing and eliminating EMI. Our surface-to-drift experiments appear to be uncontaminated by EMI.

3.4. EXPERIMENTS AT NATIONAL UNDERGROUND STORAGE, INC.

3.4.1. Location and Site Description

National Underground Storage, Inc. (NUS) is located approximately 55 mi north of Pittsburgh, Pennsylvania, in a former limestone mine. Since 1953, the facility has been used for storing documents for the many clients of NUS. The location of NUS is shown on the map of Fig. 28.

The developed part of NUS is about 61 m (200 ft) below the surface. However, we worked in an undeveloped area approximately 24 m (80 ft) below the surface. We had hoped that our isolation from electrical wiring, machinery,

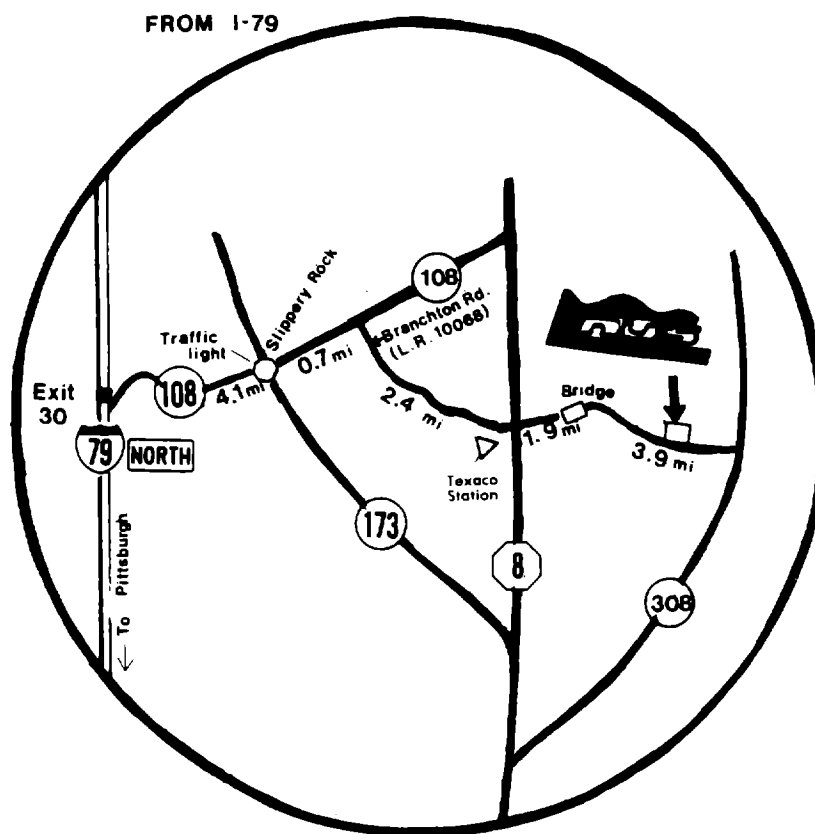


Figure 28. Map showing the location of National Underground Storage, Inc.

buried pipes, and so on would help to eliminate sneak paths and EMI. Figure 29 shows a plan view of the work area.

3.4.2. Summary of Experiments at NUS

All experiments at NUS employed surface transmitters and subsurface receivers. We used the same antennas and electronics used at LLL. The vertical distance to the surface from the receiver station was estimated to be 25 ± 3.4 m (82 ± 11 ft).

We located our transmitter antennas and electronics by using the map shown in Fig. 29 along with the reference points marked by the generator room and the borehole as shown. Using the baseline established by the generator room and borehole, we laid out a reference line 400 ft in length at 90.5° to the baseline. We located reference point A at the end of this line. If one allows for an angular error of $\pm 5^\circ$ and an error in distance of ± 3.1 m (± 10 ft), then it is expected that the point A will lie inside the cross-hatched area shown in Fig. 30. These errors are reasonable given the nature of the topography and vegetation, and the simple equipment used (Brunson compass and tape measure). The expected uncertainty in the location of point A will be important in the results to follow.

3.4.3. Experimental Results and Discussion

We performed two experiments using 100-ft-square transmitter loops. One corner of this loop was located at point A, and one side of the loop extended along our reference line between 122 m (400 ft) and 152 m (500 ft) from the borehole. Unfortunately, the length of the transmission path is only 25 m

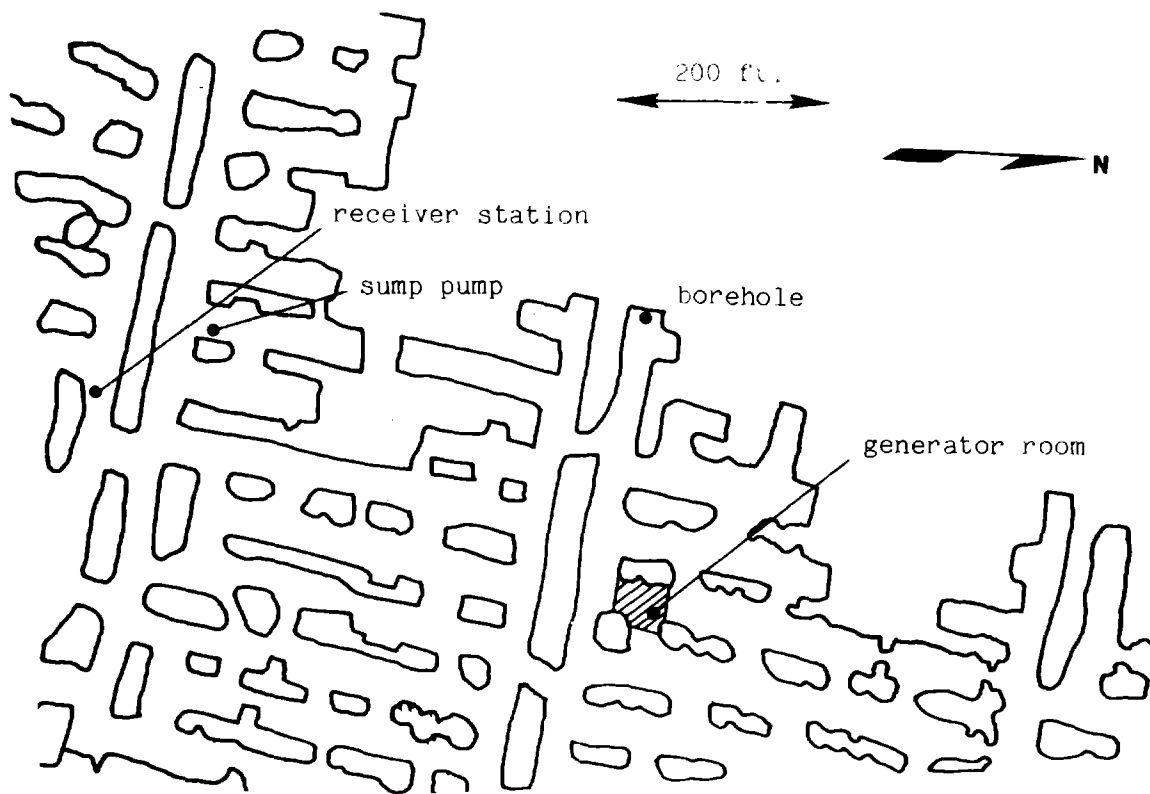


Figure 29. Plan view of the workings at NUS showing some of the features used for location.

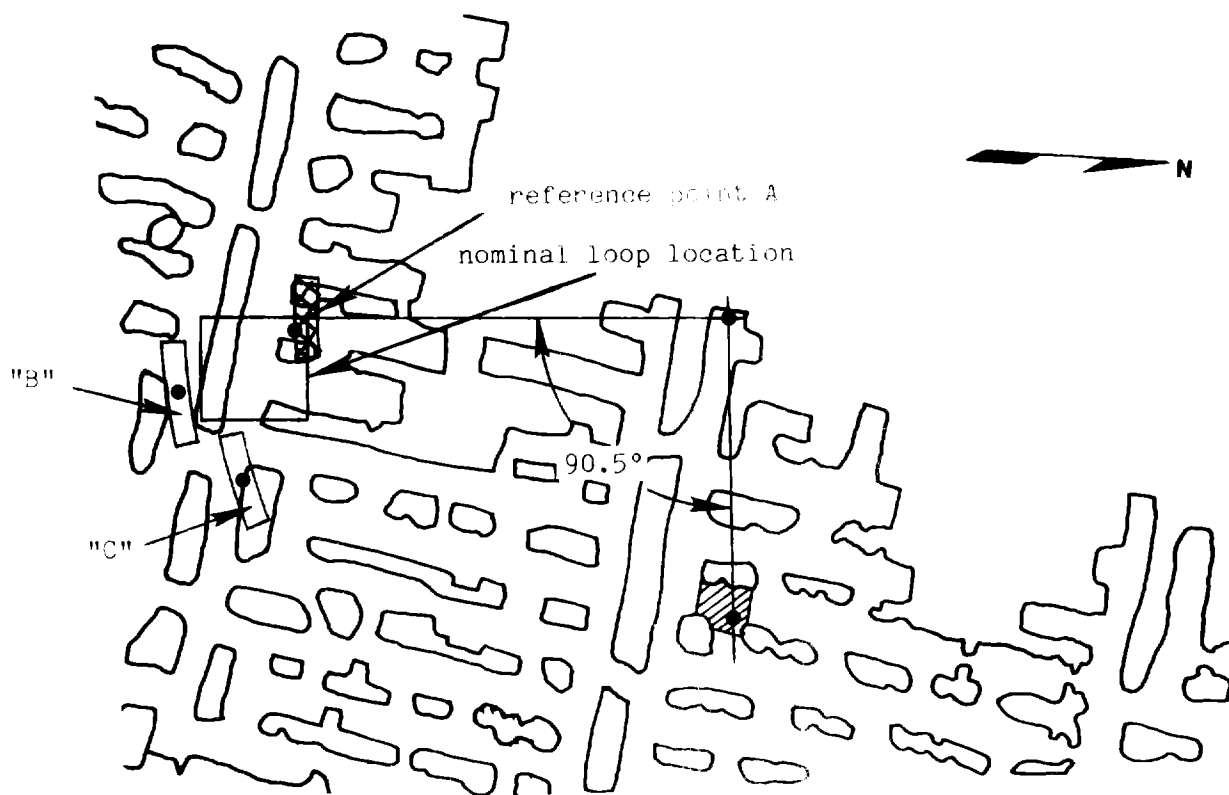


Figure 30. Plan view of the workings at NUS showing the nominal location of the 100-ft-square loop, reference point A and its region of uncertainty, region of uncertainty B, and region of uncertainty C.

(82 ft), and thus the unit magnetic dipole approximation used in our computer code will be in error. This approximation requires that the separation between transmitter and receiver be at least three loop diameters. Because the unit dipole approximation is not valid, our computer modeling for data interpretation becomes much more difficult.

We could model the problem in full by actually simulating the four sides of the loop, but with the receiver station as close to the loop as it is here, we would need to know the exact receiver location relative to each of the four sides of the loop. Given the uncertainties present in our location scheme, it would seem impossible to know the receiver location precisely enough to perform accurate modeling. We already have one free parameter in our codes (the electrical conductivity), and the addition of position as another parameter would only aggravate the difficulty. We feel the expenditure of manpower and computer time to attempt a match between computer calculations and experimental data for these cases is unwarranted.

In the next set of experiments, we located our transmitter relative to the 100-ft loop so as to place it directly above the receiver station. In reality, the location of the transmitter station is somewhere in the area marked "B" in Fig. 30. The transmitter antenna was the 64-in-square, 4-turn loop driven by the GR 1308 oscillator/amplifier. The axis of the loop was parallel to the reference line. We used EMS probes at the receiver station. The transmitter and receiver stations were connected by fiber-optic links for the voice and phase-reference signals.

We measured the vertical (z) and radial (x) components of the magnetic field. We plot the magnitude and phase of H_z in Figs. 31 and 32,

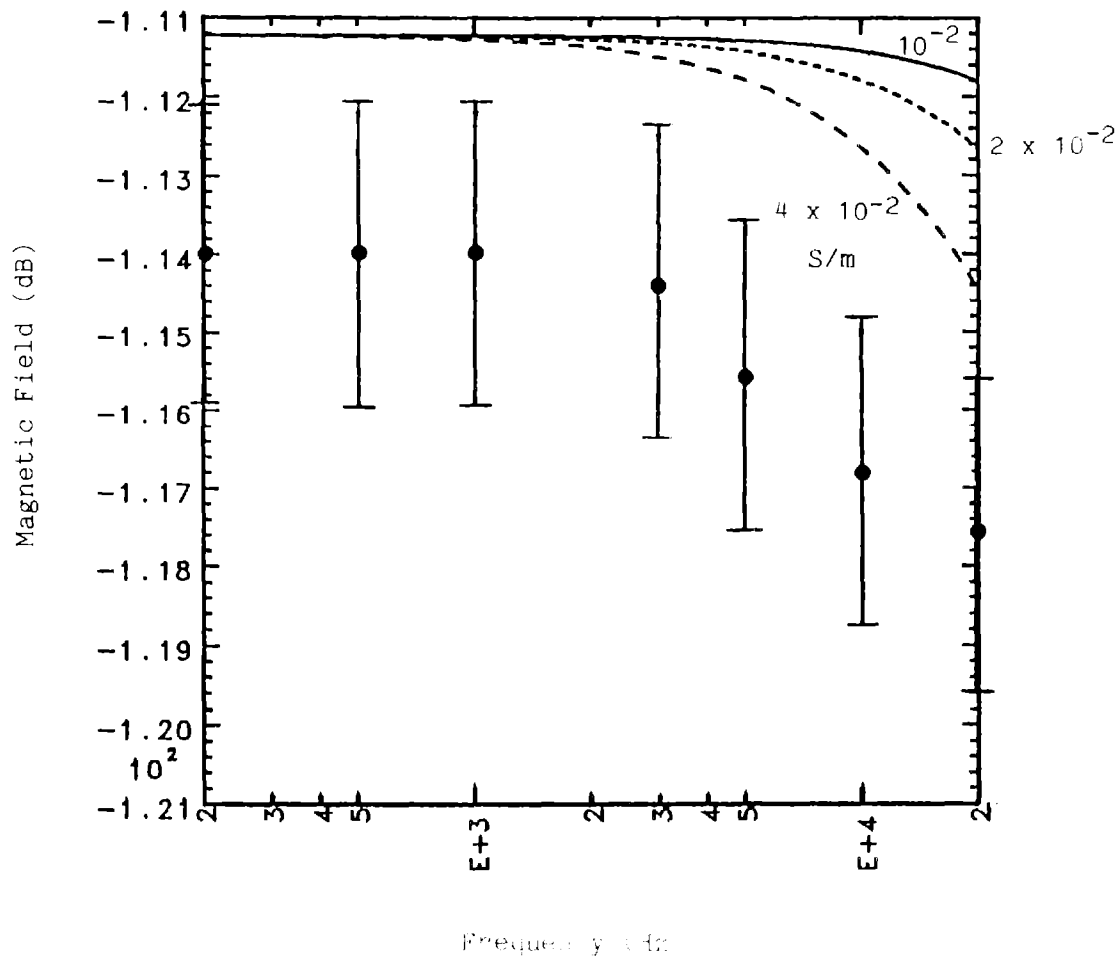


Figure 31. Magnitude of the magnetic field H_z versus frequency for transmission through 28 m (92 ft) of limestone at NUS. Computed curves are shown for $D = 20$ m (66 ft) and conductivity = 10^{-2} , 2×10^{-2} , and 4×10^{-2} S/m.

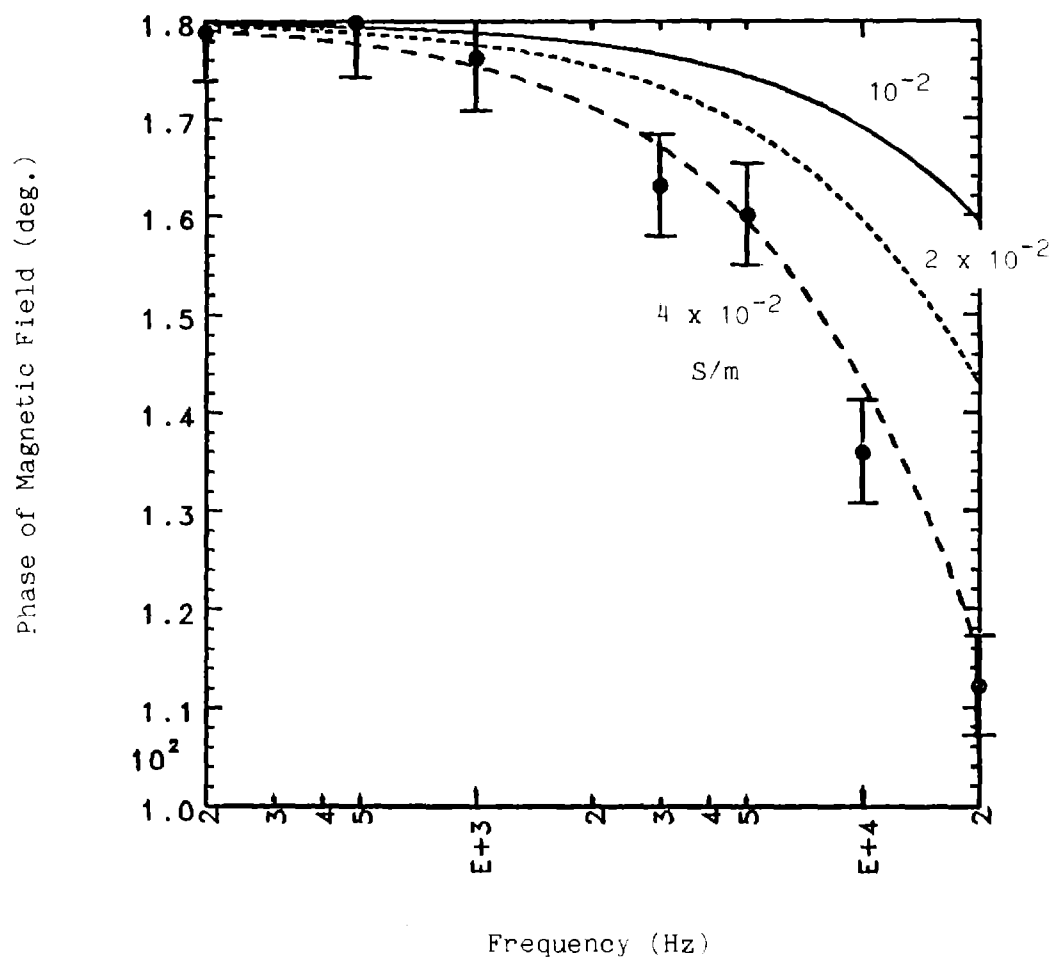


Figure 32. Phase of the magnetic field H_z versus frequency for transmission through 28 m of limestone at NUS. Computed curves are shown for $D = 20$ m and conductivity = 10^{-2} , 2×10^{-2} , and 4×10^{-2} S/m.

respectively. The experimental data are shown as dots with error bars. One feature strikes the eye immediately: H_z is not zero as it should be if the transmitter were directly above the receiver. In fact, it is even larger than H_x ! This can happen only when the receiver is not directly below the transmitter. Thus, in our computer modeling of this experiment, we include the distance D from the z axis to the receiver station as a parameter. We hope to achieve reasonable agreement between our experiments and computer calculations with the distance D no larger than the uncertainty of position from Fig. 30, about 18.2 m (59.7 ft).

We choose to fit only the curve of H_z vs frequency because the z component is relatively insensitive to misalignment of the probe, while the x component is extremely sensitive. In Figs. 31 and 32 we show computer-generated plots for a depth of 28 m (92 ft), $D = 20$ m (66 ft) and conductivities of 10^{-2} , 2×10^{-2} , and 4×10^{-2} S/m. The agreement for the phase plots is excellent if we assume that the conductivity is 4×10^{-2} S/m. The agreement for the magnitude plots is within 2 dB over the frequency range 200 Hz-20 kHz when the conductivity is chosen to be 4×10^{-2} S/m. EMI does not appear to be a problem here.

In the next set of experiments, we located our transmitter 11 m (36 ft) north and 15 m (49 ft) east of the southeast corner of the 100-ft-square loop. The figure marked "C" in Fig. 30 shows the region of uncertainty for the transmitter location. Thus, the horizontal distance between transmitter and receiver lies in the range 18-44 m (59-144 ft). The transmitter was the 64-inch-square, 4-turn loop, and the receiver was the 64-inch-square, 21-turn loop. Both loops were oriented with their axes vertically (along z).

In Figs. 33 and 34 we plot the magnitude and phase of H_z , respectively. The data are shown as dots with error bars. In Figs. 33 and 34 we also show "best fit" computer calculations using 44 m for the distance from transmitter to receiver. The computed curves are for conductivities of 10^{-2} , 2×10^{-2} , and 4×10^{-2} S/m. The data point at 100 kHz may be disregarded since the signal is artificially high due to resonance of the receiving loop. From the plots of Fig. 33, one would conclude that the conductivity is 2×10^{-2} S/m. In contrast, the data of Fig. 34 indicate a value more like 4×10^{-2} S/m.

In Figs. 35 and 36 we plot the magnitude and phase of the radial component of the magnetic field. The experimental value at 100 kHz is off scale, but again may be disregarded due to resonance in the receiving loop. The other three values do not fit any single computed curve well, but it appears that the conductivity is in the range 2×10^{-2} to 4×10^{-2} S/m. Misalignment of the receiving loop must be considered in the data interpretation since it will affect the magnitude of the received signal. For example, if our loop is misaligned by 45° , the signal magnitude will be in error by 3 dB.

In Fig. 36 we show the phase plots. Again, it appears that the conductivity lies somewhere between 2×10^{-2} and 4×10^{-2} S/m. We expect that the phase of the received signal will be less sensitive than the magnitude to misalignment.

The data of Figs. 33-36 suggest that the conductivity lies in the range 2×10^{-2} to 4×10^{-2} S/m. This is consistent with the previous data from Figs. 31 and 32.

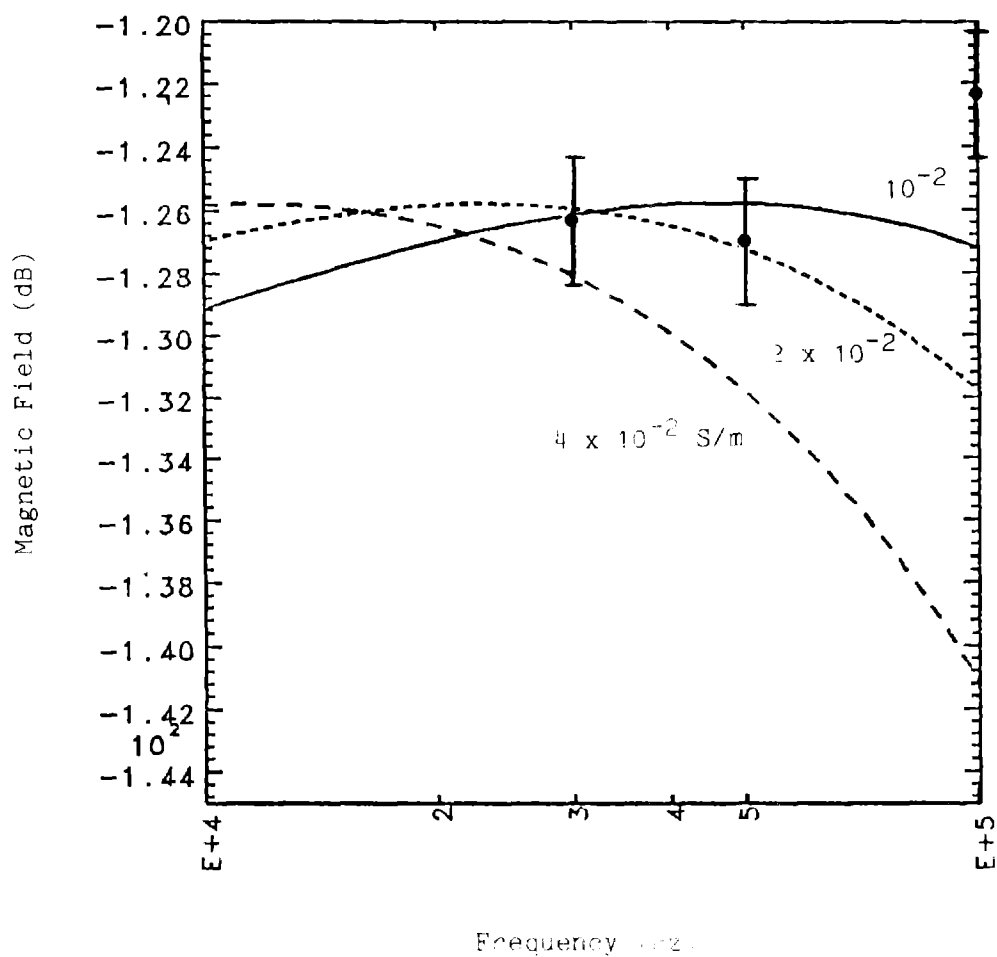


Figure 33. Magnitude of the magnetic field H_z versus frequency for transmission through 28 m of limestone at NUS. Computed curves are shown for $D = 44$ m and conductivity = 10^{-2} , 2×10^{-2} , and 4×10^{-2} S/m.

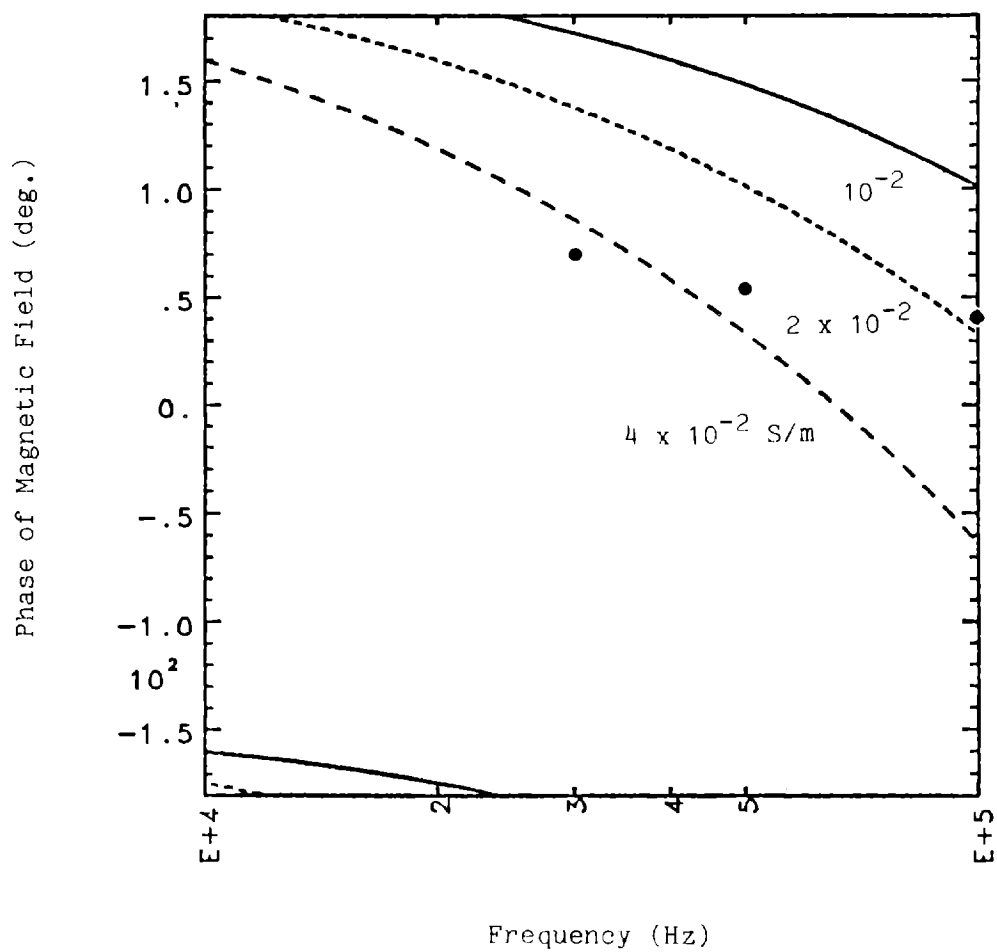


Figure 34. Phase of the magnetic field H_z versus frequency for transmission through 28 m of limestone at NUS. Computed curves are shown for $D = 44$ m and conductivity = 10^{-2} , 2×10^{-2} , and 4×10^{-2} S/m.

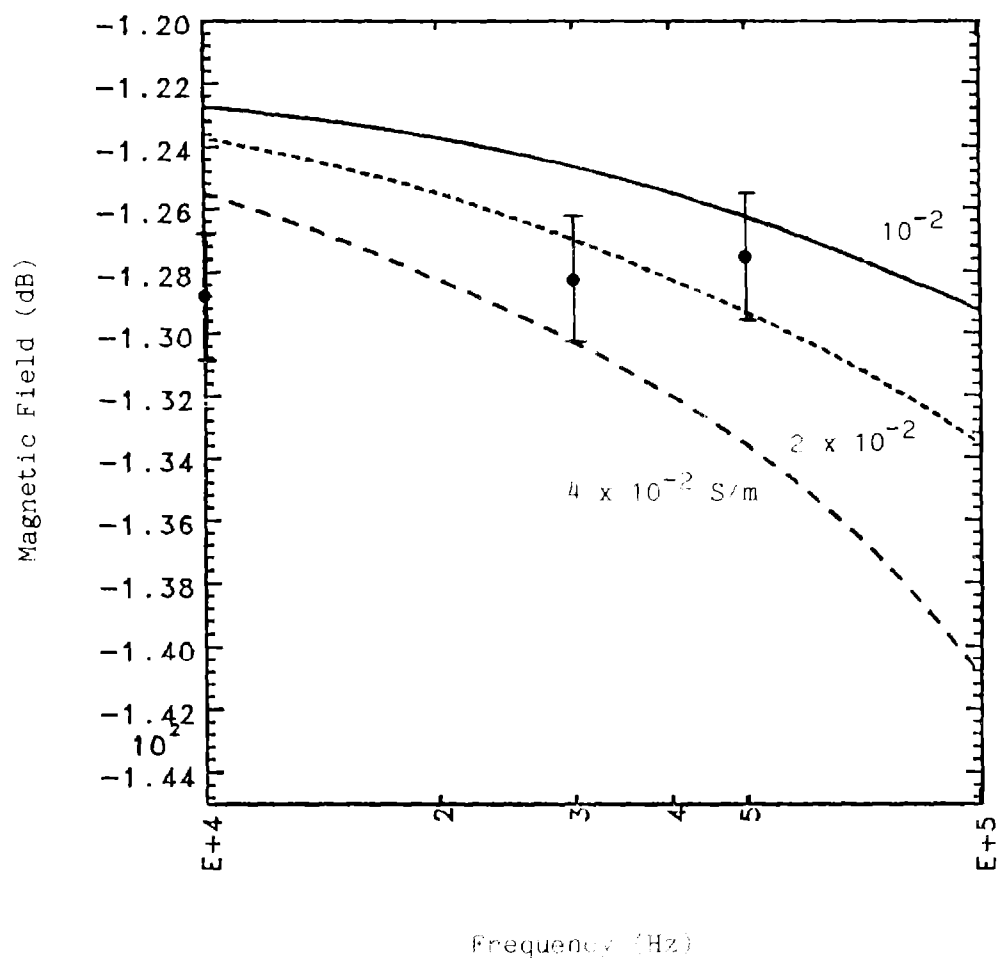


Figure 35. Magnitude of the magnetic field H_r versus frequency for transmission through 28 m of limestone at NUS. Computed curves are shown for $D = 44$ m and conductivity = 10^{-2} , 2×10^{-2} , and 4×10^{-2} S/m.

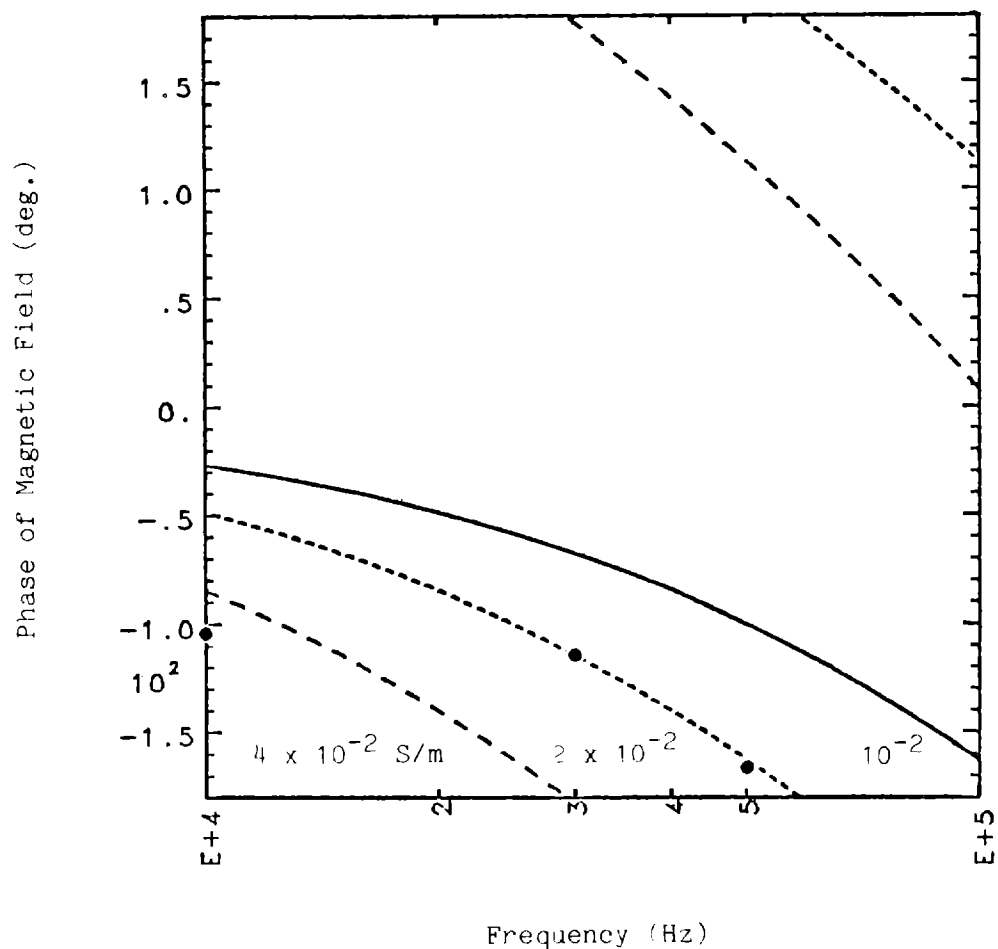


Figure 36. Phase of the magnetic field H_r versus frequency for transmission through 28 m of limestone at NUS. Computed curves are shown for $D = 44$ m and conductivity = 10^{-2} , 2×10^{-2} , and 4×10^{-2} S/m.

In our final set of experiments, we used our helical dipole transmitter on the surface and the active electric field probe or the 64-in-square, 21-turn loop as the receiver. We had some difficulty driving the helical dipole because of impedance mismatch problems. As a result, the received signals were rather weak. In addition, we have no satisfactory way to model the helical dipole with our present codes. For these reasons, we feel that it is not worth the time to present the data or attempt to match it to computer calculations.

3.4.4. An Estimate of Channel Capacity for NUS

At NUS we transmitted through small thicknesses of material, so extrapolation of the experimental data will be necessary to look at cases of interest. We take the data from Fig. 31 as our base case. The S/N ratio for this data set is plotted in Fig. 37 over the frequency range 200 Hz-20 kHz. The transmitter was again assumed to be 28 m above the receiver and 20 m away laterally. Thus, the distance between transmitter and receiver was 34.4 m.

As before, we extrapolate the data to a greater depth by use of our computer codes. We shall assume that the conductivity is 4×10^{-2} S/m, that the noise is independent of depth, and that the vertical and lateral distances between transmitter and receiver are 81.4 m (267 ft) and 58.1 m (191 ft) (straight line distance = 100 m), respectively. The extrapolated S/N ratio (lower plot) is also shown in Fig. 37.

Channel capacity can now be estimated using Figs. 25 and 37. At 81.4 m depth (100 m straight line distance), the useful bandwidth is 3 kHz if $S/N > 15$ dB. the maximum theoretical channel capacity is thus $5.03 \text{ bit/s} \cdot \text{Hz} \times 3$

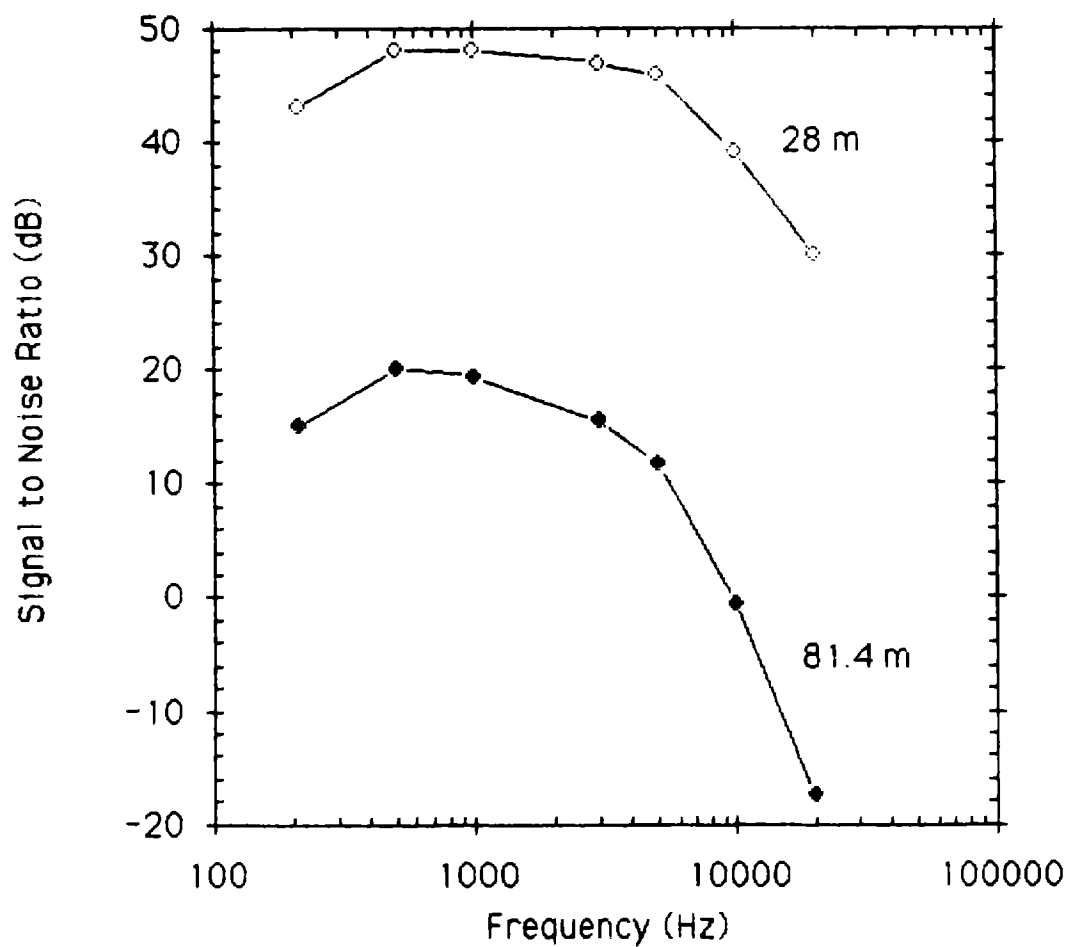


Figure 37. Actual signal to noise ratio data for transmission through 28 m of limestone at NUS (upper plot). Signal to noise ratio extrapolated to a depth of 81.4 m. It is assumed that the noise at a particular frequency is independent of depth.

kHz = 15.1 kbit/s. The reader will recall from Table I that the channel capacity at LLL was much greater (71.3 kbit/s).

The greater channel capacity at LLL should be no surprise for three reasons. First, the conductivity is lower at LLL. Second, the transmitter/receiver configuration at NUS is not optimal. Third, the current moment of the transmitter loop (current times loop area) was much larger at LLL.

3.4.5. Conclusions from Work at NUS

The in situ conductivity of the upper layers of limestone at NUS is about 4×10^{-2} S/m. This corresponds to attenuation constants of 0.034, 0.11, 0.34, and 1.1 dB/m at 100 Hz, 10 kHz, and 100 kHz, respectively.

The NUS experiment demonstrated the need for care in determining the locations of transmitters and receivers. Uncertainties in lateral location at NUS were of the same order as the thickness through which we transmitted. Interpretation of our data from NUS was made difficult because of these uncertainties.

We shall also need to develop better ways of orienting our field probes to minimize the effects of misalignment. There are situations where a few degrees of misalignment can result in grossly inaccurate measured values.

4. CONCLUDING REMARKS

The computer modeling and experimental work performed under the Air Force contract in 1984 achieved some promising results. The basic modeling requirements of evaluating conductivity and air-earth interface effects were

achieved. Prompted by inquiries from the Air Force and its contractors, we went on to evaluate multilayered effects and started to evaluate wire insulator effects. Early in the experimental work, it became apparent that we would have to develop a means of verifying that the signal propagates through rock and not by some unsuspected path to the surface-based receivers. In October, 1984, we utilized methods for evaluation of propagation through limestone and interbedded sedimentary formations at the Lake Lynn Laboratory (LLL) and the National Underground Storage (NUS) facility and found that "sneak through" paths existed for some of the experimental arrangements that allowed greater signal strengths to propagate than could be expected from pure through-the-Earth communication. However, our methodology also demonstrated when propagation was predominately through the Earth. These results were consistent with computer-generated models, and attenuation and conductivity parameters were estimated for the rock.

Estimates for maximum channel capacity, based on our experimental data, were made for transmitter depths of 100 m to 500 m. Results up to 300 m are very promising, with theoretical channel capacities of the order of kbits/s for a modest transmitter size. However, these estimates represent a maximum under a specific set of assumptions. Actual channel capacities will depend upon the noise figure and type, and the specific geologic and environmental settings. Also, the achievable bit rate and bit error rate are a function of the modulation scheme used to transmit the binary information. However, these results do indicate that the minimum information rate of 75 bits/s should easily be achieved.

Further work is planned for FY85. This includes additional computer model developments and a field experiment with a subsurface to surface distance greater than 305 m (1000 ft).

5. ACKNOWLEDGMENTS

We wish to acknowledge the generous support of the Headquarters of the Ballistic Missile Office (HQ BMO) at Norton Air Force Base for this work. Also, the authors express their appreciation to Lt. Durrall Carroll and Lt. Mohammed Faruk of the U.S. Air Force, and Dave Edwards of TRW-San Bernardino for their constructive comments and assistance in this research. We also appreciate the assistance of Robert Mattes of the U.S. Bureau of Mines at Lake Lynn Research Laboratory, David Sansom of the National Underground Storage, Inc., and Dr. Jan van Wagtendonk of the National Park Service at Yosemite National Park in providing sites for our field experiments. Also, we acknowledge Dan Bukofzer of Lawrence Livermore National Laboratory/Naval Post Graduate School (Monterey) for his helpful comments. Last, but not least, we acknowledge Ray Egbert of the Lawrence Livermore National Laboratory for his excellent technical assistance in the field.

6. REFERENCES

1. A. Banos, Dipole Radiation in the Presence of a Conducting Half Space (New York: Pergamon Press, 1966).

2. G. J. Burke and E. K. Miller, "Modeling Antennas Near To and Penetrating a Lossy Interface," IEEE Trans. Antennas Propag. AP-32 (1984).
3. G. J. Burke, C. Dease, E. M. Didwall, and R. J. Lytle, "Numerical Modeling of Subsurface Communication," Lawrence Livermore National Laboratory, Livermore, Calif., in progress.
4. A. W. Guy and G. Hasserjian, "Impedance Properties of Large Subsurface Antenna Arrays," IEEE Trans. Antennas Propag. AP-11 (1963).
5. R. W. P. King and G. S. Smith, Antennas in Matter (MIT Press, Cambridge, MA, 1981).
6. R. J. Lytle and D. L. Lager, "Numerical Evaluation of Sommerfeld Integrals," Lawrence Livermore National Laboratory, Livermore, Calif., Report UCRL-51688 (1984).
7. E. K. Miller, "A Variable Interval Width Quadrature Technique Based on Romberg's Method," J of Comput. Phys. 5 (1970).
8. J. H. Richmond and E. H. Newman, "Dielectric Coated Wire Antennas," Radio Sci. 11 (1976).
9. C. H. Stoyer, "Electromagnetic Fields of Dipoles in Stratified Media," IEEE Trans. Antennas Propag. AP25 (1977).

10. J. R. Wait, "Propagation of Radiowaves Over a Stratified Ground,"
Geophysics 18 (1953).
11. J. R. Wait, "The Magnetic Dipole Antenna Immersed in a Conducting
Medium," Proc. IRE 40 (1952).